UNIVERSITÀ
DEGLI STUDI
DI PADOVA

DIPARTIMENTO
DI INGEGNERIA
DELL'INFORMAZIONE

MASTER THESIS IN ELECTRONIC ENGINEERING

# Speed control of hybrid excitation permanent magnet motor.

MASTER CANDIDATE

**Filomena Pascariello**

**Student ID 2050313**

SUPERVISOR

**Prof. Nicola Bianchi**

**University of Padova**

CO-SUPERVISOR

**Dott.ssa Chiara Contò**

**Dott. Fabio Filippini**

**Dott. Francesco Tripaldi**

**University of Padova**

ACADEMIC YEAR
2023/2024

*So close no matter how far*
*can get much more from the heart*
*forever trust in who we are*
*and nothing else matters...*

# Abstract

This thesis focuses on the design and testing of a control drive for a *Hybrid Excited Permanent Magnet (HEPM)* motor, addressing both theoretical and experimental aspects.
The study begins with an overview of electric motors,highlighting the need for new solutions because of environmental and geopolitical concerns related to *Rare Earth Elements (REEs)* extraction. The HEPM motor is proposed as the solution under study. The key advantage of this motor is its ability to vary rotor flux, improving the performance in terms of speed, torque, and power density.
Both linear and non-linear models are developed, and the control scheme is designed, with particular emphasis on *Flux Weakening (FW)* operation. The entire system is simulated and optimized, taking into account two different types of reference signals: a step and a ramp. Then speed, currents and torque results are showed. Moreover, an improvement for the *Maximum Torque per Ampere (MTPA)* strategy is proposed with the aim of improving the torque ability to track the reference signal.
Then experimental tests are carried out an a motor prototype, both with and without the improved MTPA strategy. Test results are consistent with those obtained during simulation.
Further enhancements were achieved through optimization of the rotor alignment procedure. By combining the enhanced MTPA strategy with the optimized rotor alignment procedure, the test results demonstrate a significant improvement in performance.

# List of Figures

# List of Tables

# Contents

# Glossary

**ADAS** Advanced Driver Assistant Systems. 2

**BEMF** Back Electro-Motive Force. 35

**EESM** Electrically Excited Synchronous Motor. 6

**EV** Electric Vehicles. 1

**FE** Finite Element. 63

**FEA** Finite Element Analysis. 27

**FW** Flux Weakening. 17

**HEPM** Hybrid Excited Permanent Magnet. 7

**IC** Internal Combustion. 2

**IPM** Interior Permanent Magnets Motor. 5

**LPF** Low Pass Filter. 41

**LUT** Look Up Table. 37

**MTPA** Maximum Torque Per Ampere. 16

**NdFeB** Neodymium, Iron and Boron alloy. 6

**ODE** Ordinary Differential Equation. 30

**PMs** Permanent Magnets. 4

**PMSMs** Permanent Magnet Synchronous Motors. 4

**REEs** Rare Earth Elements. 6

**SPM** Surface- Mounted Permanent Magnets Motor. 4

**SVM** Space Vector Modulation. 64

# 1

# Introduction

Nowadays all our technology resources are employed to solve an important problem: climate change. One of the major components of environmental pollution is coming from transportation emissions and, switching to electric, becomes almost a necessity. In this Chapter, we are going to shortly deal with electric vehicle history and structure, stressing the reasons why is important to find more sustainable alternatives.

## 1.1 HISTORY

*Electric Vehicles (EV)* are introduced more than 100 years ago. It is hard to pinpoint the invention of the electric car to one inventor or country since it is a result of a technological progress started with the invention of battery till electric motor. The first very successful electric car is dated to 1890 with William Morrison: he created an electrified wagon for 6 passengers with a top speed of 14 miles per hour (about 23 km/h)[1]. After that, there is a big outbreak for electric vehicles in few years (more than a third of all vehicles on the road were electric) and to understand their outspread it is important to consider that, aside from horses, the other means of transport available in that age are steam and gasoline vehicles. Steam propulsion turns out to be a very good solution when it comes to trains and factories but for cars it has a lot of drawbacks: they require long start up times and they need to be refilled with water, limiting their range. Gasoline vehicles have long starting time too since they need to be manually propelled with a hand crank and they are not easy to drive due to the presence of the gear changing system. These types of vehicles are also considered kind of dirty since the engine is not clean as the electric one, they are noisy and their exhaust is unpleasant [2]. So, EVs are the best choice but, on the other hand, EVs are expensive. They are not made for the everybody but only for the upper class.

With time also the *Internal Combustion (IC)* technologies are developed and the widespread of electric vehicles end; in the following the reasons why this happened are explained:

- EVs are used for short trips around the city but by the 1920s, street started to be more developed connecting different cities; to reach one-another, vehicles have to perform in a longer-range that EVs are not able to fulfil.
- The discovery of oil reduces the price of gasoline making it affordable to the average consumer.
- The invention of an electric starter substituting the hand crank.
- The starting of mass-production by Henry Ford putting on the market the fist internal combustion car (Model T in 1908) that is affordable, more than electric cars.

New interest in EVs is born after the second half of the 19th century, with few starts and stops : alternative-fuelled vehicles are considered to reduce problems coming from emissions of IC engines and to reduce the dependence on oil. Development efforts of electric vehicles are renewed thanks to several legislative and regulatory actions. From this, automobile manufacturers spend their resources trying to develop better solutions in terms of costs, materials and driving range. Several solutions are proposed making step forward also on batteries technology in terms of weight (recent batteries are lighter than ancient ones) and energy density using new chemistry (such as NiMH and lithium ion). The full breakout happens in the 21st century thanks to Toyota that put on the market a hybrid car called Prius. Soon after Toyota, there is the founding of Tesla with the porpoise to build full electric vehicles.

Nowadays, the rise of oil price and the increase of carbon pollution seals the come back of electric cars and companies started again investing in electric solutions to counteract the negative effects of emissions. Moreover, thanks to the enhancement of power electronics and electro-mechanical devices, EVs are becoming more and more efficient: traction of the electric motor drive is optimized, the driving experience inside the vehicle is improved not only with *Advanced Driver Assistant Systems (ADAS)* but also with robotic application making the vehicle more autonomous.

## 1.2 OVERVIEW OF AUTOMOTIVE VEHICLES TECHNOLOGIES

An EV is a vehicle propelled totally or partially by an electric energy source. Electric energy is converted in mechanical energy without any polluting waste material. On contrary to IC vehicles, energy conversion happens through a thermal combustion with the generation of fumes as waste materials.

Electric technology can be broken down into three types:

- **Hybrid Electric Vehicle**: all the energy used to propel the vehicle is coming from IC; battery is charged by the combustion of gasoline and regenerative braking. The electric motor provides propulsion assistance or all-electric propulsion at low speeds.
- **Battery Electric Vehicle**: only electricity as fuel, making it a full electric vehicle; it must be recharged by plugging it to the grid.
- **Plug-in Hybrid Vehicle**: gasoline and electricity propel the vehicle in a blended mode or gasoline engine operates only when battery is low charge.

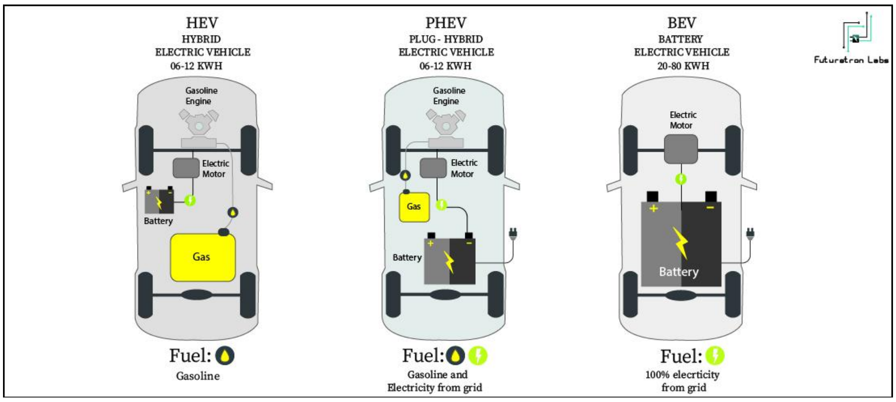

Figure 1.1: HEV, PHEV and BEV powertrain configuration.[3]

Hybrid technology is growing reaching good level of competition with combustion engines, but the main objective is to switch to full-electric. Fig.(1.2) shows the an EV scheme:

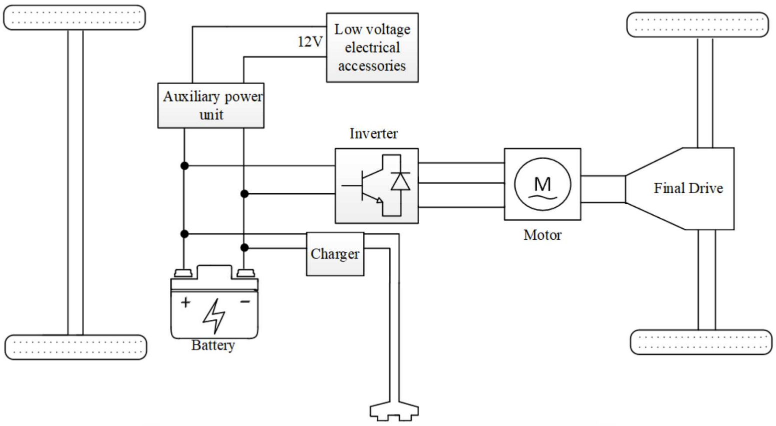

Figure 1.2: EVs power-train.[4]

An electric motor is composed of two mechanical parts, a rotating part called rotor and a static part called stator, and two electrical parts, field magnets and armature windings that are attached one to the rotor, the other one to the stator.

Depending on the position of the stator respect to the rotor, different configurations can be discriminated: outer rotor motor, where the stator is placed inside the rotor; inner rotor motor, instead, has the stator placed outside the rotor. In the last case, stator surrounds the rotor with an air gap as small as possible not to compromise the performance but large enough to enable the rotation. In the air gap, through rotation, torque is generated. In Fig.1.3 an example of inner rotor motor is shown.

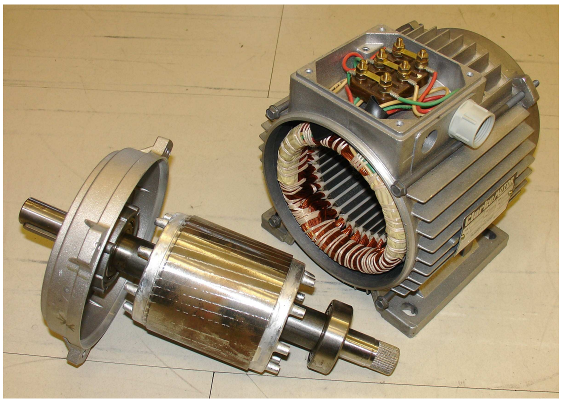

Figure 1.3: Example of a rotor (on the left) and a stator (on the right).[5]

There are different kind of electric motors on the market but not every type is suitable for automotive traction since there are precise requirements to fulfil: high torque, high power, a wide constant power region, compact size and reduced weight. *Permanent Magnet Synchronous Motors (PMSMs)* stand out as a commonly favoured option for traction applications.

## 1.3 Electric Motors

An electric motor is a machine performing the electro-mechanical conversion of the energy. Synchronous motors are the state of art in automotive application and they are characterized by the fact that rotation speed of the rotor is the same of magnetic field generated by stator windings. In fact, thanks to the high magnetizing field generated by *Permanent Magnets (PMs)*, they provide a high torque and power density. Synchronous motor can be furtherly classified in *PM* motors and *PM-less* motors.

### 1.3.1 PM Motors

In PMSMs, rotor field is generated by PMs mounted on the surface of the motor (*Surface-Mounted PM Motor*) or buried in the rotor (*Interior PM Motor*). SPM motors dominated the market of PM motors but, in recent years, EVs market requires motors with higher torque and power over a wider speed range with

higher efficiency. So the actual choice is IPM motor.
To better understand the differences between them, we can make a comparison:

- in **SPM motors**, there are magnets mounted on the exterior surface of the rotor, so rotor field paths along the *d*-*q* axes are almost the same, meaning that the inductances along the axes are:

  $$L_d \approx L_q$$

  This results in a limited saliency and SPM motors can rely only on the magnetic component of the torque.

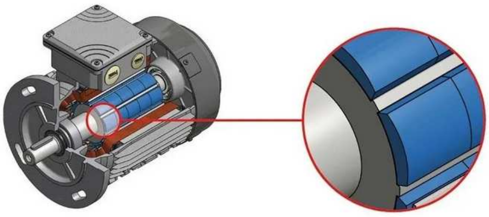

Figure 1.4: SPM motor.[6]

- in **IPM motors**, magnets are placed inside in the rotor itself, so the mechanical strength is higher respect to the one of the SPM, resulting in higher operating mechanical speeds. Since PMs are inside the rotor, the inductances along the *d*-*q* axes are not the same:

  $$L_d < L_q$$

  in this way, saliency is higher and the motor can rely, both on a magnetic component and a reluctance component of the torque.

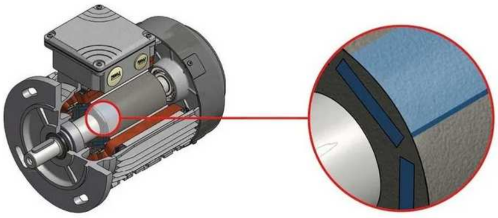

Figure 1.5: IPM motor.[6]

Thanks to the reluctance component of the torque, IPMs can have a lower percentage of PMs with respect to SPMs and a wider speed range.

### 1.3.2 Rare Earth Materials Issues

IPM motors have huge drawback: PMs inside the rotor are made of *REEs*, a gathering of elements that are present in earth's crust in low concentration. Magnets are mostly *NdFeB* magnets, an alloy of Neodymium, Iron and Boron plus Dysprosium to increase temperature stability. They are the best performing type of PMs because of their resistance to de-magnetization (they can be polarized in any direction) and because they generate the highest magnetizing flux, compared to other magnetic materials. However, the extraction and manufacturing of PM materials imply environmental and geopolitical issues [7]:

1. The demand of REEs increases and it is projected to spike in up coming years as industries are investing in clean energy. The matter with REEs starts from the extraction process. There are two primary methods: drilling and chemical erosion. Both methods produce toxic waste contaminating air, water and soil.

2. There are only few countries active in extraction, the monopoly is held by countries in which the concentration in soil is higher.

3. Soon there will be a shortage and,consequently, cost increase.

To counteract the negative backlash of REEs, different solutions can be proposed: to reduce the concentration of REEs used in electronic components and motors, to develop recycling programs of REEs, and to diversificate the sources reducing the hold of only few countries. One possibility is to design motors with reduced magnetic material or even no PMs at all. Different motor topologies are proposed in the following section.

### 1.3.3 Alternatives to PM Motors

In this section two topologies are presented as an alternative to PM motors. They are motors in which PMs are partially or completely absent in the rotor. The design of this kind of motors is interesting for their performance. In fact, they overcome one of PMSM limitations. In PM motors, PM flux has to be increased to enhance power density, worsing high speed capabilities.
Two configurations are taken into account:

- **Electrically Excited Synchronous Motor (EESM)** : on the rotor are placed windings instead of PMs. The possibility to regulate rotor current provides an additional degree of freedom. In fact, the current is directly related to the rotor magnetizing flux generated. Such flux can be modulated as desired, with various advantages such as: adaptable power factor control, high efficiency in a wide operating range and constant power-speed range. However, windings generate additional copper losses that decrease efficiency and generate heat. Thermal managment can be challenging for such machines. Fig.1.6 shows a EESM with a salient pole rotor structure.

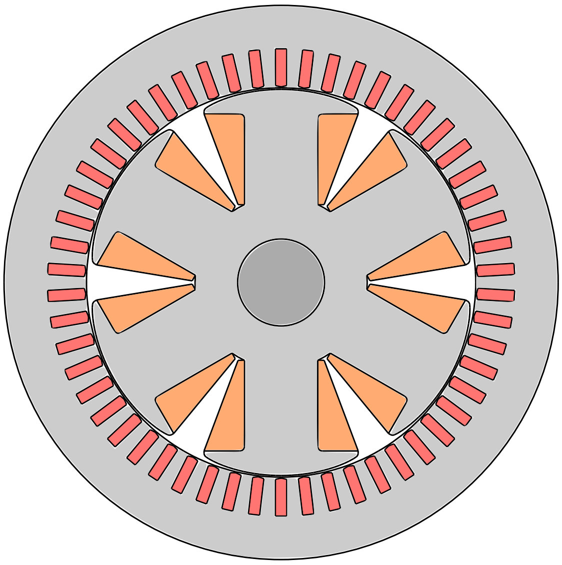

Figure 1.6: EESM motor.[8]

- **Hybrid Excited Permanent Magnet (HEPM) motor**: made of a hybrid rotor structure with both windings and PMs. Fig.1.7 two PMs inserted in each pole shoe of an EESM. Additional PMs allows for an increase of torque and power density, with respect to EESM motors. This can also reduce the required rotor excitation current, thus limiting the heat generation.

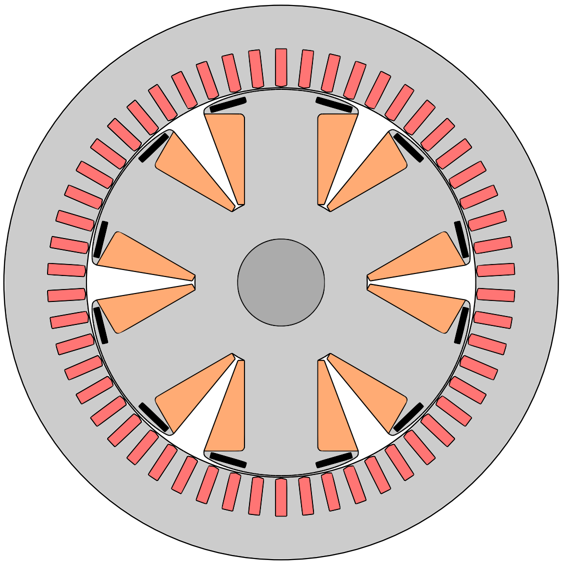

Figure 1.7: HEPM motor.[8]

A comparison between these two motors is presented in [8]. Some simulations can be carried out to compare EESM and HEPM motors.

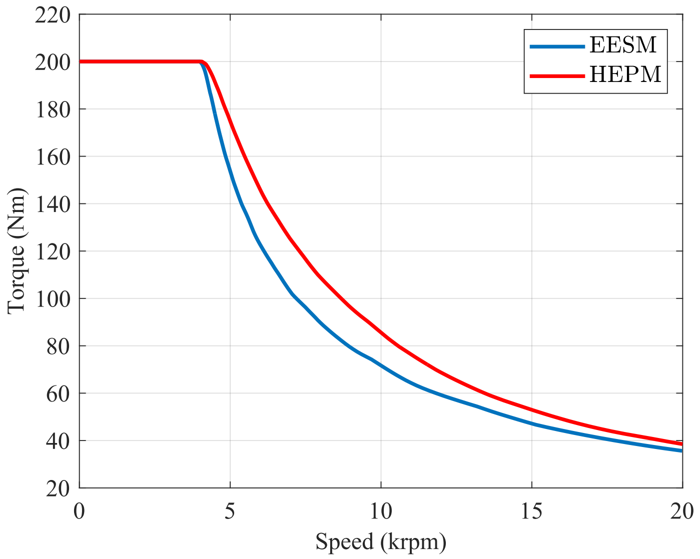

Figure 1.8: Torque comparison between PM-less motors.

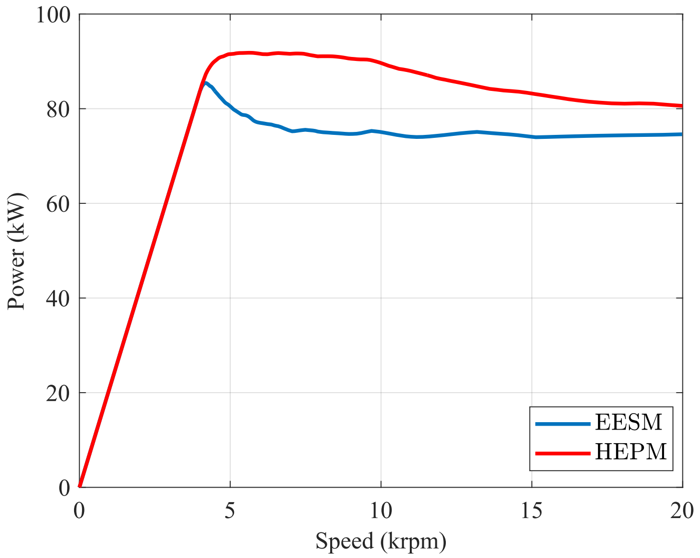

Figure 1.9: Power comparison between PM-less motors.

When it comes to torque and power capabilities, shown in Fig.1.8 and 1.9 all motors have similar performances at low speed while during FW operation they behave in different ways. During FW, EESM motor is able to keep high torque density but power is not constant. Differently HEPM motor power is higher and almost after its maximum. In conclusion, the HEPM motor presented is an improved version of EESM since the addition of a small amount of PMs results in a significant enhancement in performance. For this reason, this study focuses on HEPM motors.

## 1.4 Objective of the Thesis

The objective of this thesis is to analyse and design the control of one of the possible alternatives to PMSMs: a *Hybrid Excitated Permanent Magnet motor*. The study is carried out by modeling the behaviour of the motor and control thanks to Matlab Simulink simulation tool. Afterwards, results coming from simulation are validated with tests carried out on the experimental bench.

# 2

# Hybrid Excited Permanent Magnet motor

This chapter deal with the HEPM motor under analysis. First, its design and configuration are presented. Then, its operating conditions are discussed. At last, a deeper look is given to the design of a strategy to vary the rotor flux with excitation windings.

## 2.1 HEPM GEOMETRY AND PROTOTYPE

HEPM motor is a combination of a PM motor and an EESM due to the presence of both PMs and excitation winding. It can be obtained starting from a PM motor substituting or adding coils alongside with PMs. Fig. 2.1 shows two main topologies:

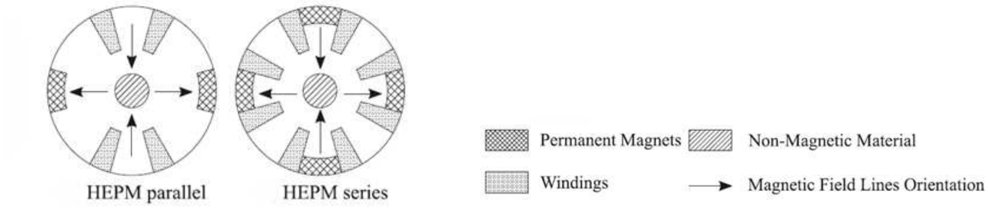

Figure 2.1: HEPM rotor configurations with element legend.[9]

- **Series Configuration**: rotor windings are placed around PMs, sharing the same path for the flux.

- **Parallel Configuration**: alternatives PM poles are replaced by coils, generating two different flux paths in the rotor.

Studies [10] show that series configuration has more disvantages respect to the parallel one. The series configuration shows significant losses at high speed that can effect machine efficiency. So, the parallel configuration is the one choosen for the HEPM motor.

### 2.1.1 Motor Under Study

Fig.2.2 shows rotor and stator of the HEPM motor prototype. The winding in the rotor of Fig. 2.2a are missing to highlight the presence of magnets.

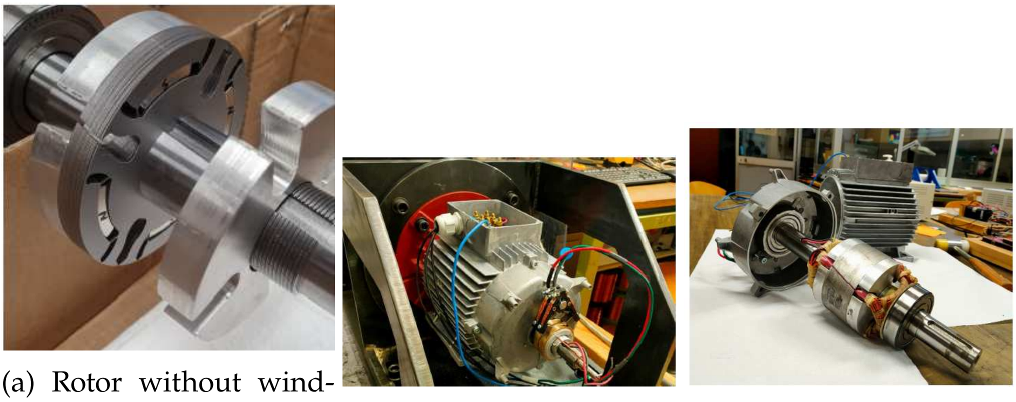

(a) Rotor without windings. (b) Casing. (c) Rotor assembly.

Figure 2.2: HEPM motor prototype.[11]

This motor is characterized by the following parameters, Table 2.1:

| Absolute values | | Nominal Values |
|---|---|---|
| $2p = 4$ | $\lambda_m = 0.6755\ Vs$ | $DC\ Bus = 300\ V$ |
| $R_s = 20.15\ \Omega$ | $R_e = 4.15\ \Omega$ | $V_N = 175\ V$ |
| $L_d = 0.157\ H$ | $L_e = 0.308\ H$ | $I_N = 2\ A$ |
| $L_q = 0.486\ H$ | $M_e = 0.058\ H$ | $I_{eN} = 3\ A$ |

Table 2.1: Motor Parameters.

Nominal voltage peak value is computed from the DC Bus voltage as:

$$V_N = \frac{DC\ Bus}{\sqrt{3}}$$

considering a stator connected winding and the PWM inverter control.

## 2.2 Operating Conditions

The HEPM motor operating conditions are computed. Starting from motor equations, *current limit*, the *voltage limit* and *torque limit*.

Thus, motor equations are presented in this section and then current, voltage and torque limits are computed.

### 2.2.1 MOTOR MODEL

To describe the motor model, the rotating *d*-*q* reference frame is adopted. In particular, this reference frame is synchronous with the rotor. The direct axis is aligned with the PM flux. Considering such reference frame, the stator and rotor voltage equations are:

$$v_d = R_s i_d + \frac{d\lambda_d}{dt} - \omega_{me}\lambda_q \tag{2.1}$$

$$v_q = R_s i_q + \frac{d\lambda_q}{dt} + \omega_{me}\lambda_d \tag{2.2}$$

$$v_e = R_e i_e + \frac{d\lambda_e}{dt} \tag{2.3}$$

where $v_{d,q,e}$ , $i_{d,q,e}$ , $L_{d,q,e}$ are respectively direct, quadrature, excitation voltages, currents and inductances, respectively. $R_{s,e}$ are stator and excitation resistances, $\Lambda_m$ is the constant PM flux linkage, $\omega_{me}$ is the electro-mechanical rotating speed. The motor, in this set of equations, is considered magnetically linear and cross saturation effects are neglected. Flux linkages are defined as:

$$\lambda_d = \Lambda_{pm} + L_d i_d + M_e i_e \tag{2.4}$$

$$\lambda_q = L_q i_q \tag{2.5}$$

$$\lambda_e = L_e i_e + \frac{3}{2} M_e i_d \tag{2.6}$$

where $\Lambda_{pm}$ is the PM flux linkage.

The mutual inductance $M_e$ is multiplied by $\frac{3}{2}$ in the excitation winding equation (2.3) to take into account the transformation effect from rotor to stator reference frame. Substituting (2.4) (2.5) and (2.6) in (2.1) (2.2) and (2.3) holds:

$$v_d = R_s i_d + L_d \frac{di_d}{dt} + M_e \frac{di_e}{dt} - L_q i_q \omega_{me} \tag{2.7}$$

$$v_q = R_s i_q + L_q \frac{di_q}{dt} + \omega_{me}(\Lambda_{pm} + L_d i_d + M_e i_e) \tag{2.8}$$

The HEPM motor has an additional equation (2.9) to consider the presence of the excitation windings:

$$v_e = R_e i_e + L_e \frac{di_e}{dt} + \frac{3}{2} M_e \frac{di_d}{dt} \tag{2.9}$$

Even though cross-coupling between direct and quadrature currents is presented also in PM motors, in case of hybrid motors the cross-coupling is more pronounced as direct current is not only coupled to the quadrature one, but also to the excitation current through a non negligible mutual inductance $M_e$. Moreover, the direct flux linkage $\lambda_d$ is influenced by the excitation flux, as shown from (2.4).

Torque equation can be computed, starting from HEPM motor:

$$\begin{aligned} T &= \frac{3}{2}p(\lambda_d i_q - \lambda_q i_d) \\ &= \frac{3}{2}p[\Lambda_m + M_e i_e + (L_d - L_q)i_d]i_q \end{aligned} \tag{2.10}$$

For HEPM motor an extra degree of freedom can be exploited: variations in excitation current bring changes on direct current and torque, giving the possibility to directly act on the operating points.

## 2.2.2 CURRENT AND VOLTAGE LIMITS

Current and voltage supplied to the motor are generated by the inverter. To design efficiently the motor and its control, currents and voltages required by the motor should not exceed inverter limits, not to cause faults and damages to the system. The current limits is described by the following equation:

$$I_N^2 = I_d^2 + I_q^2 \tag{2.11}$$

where $I_N$ is the nominal current of the motor. This equation describes a circle in the $d$-$q$ plane, centered in its origin.

The voltage limit is:

$$V_N^2 = V_d^2 + V_q^2 \tag{2.12}$$

where $V_N$ is the nominal voltage of the motor. Direct and quadrature voltages can be retrieved from (2.1) and (2.2), obtaining:

$$V_N^2 = R_s^2(I_d^2 + I_q^2) + \omega_{me}^2[(\lambda_{he} + L_d i_d)^2 + (L_q I_q)^2] \tag{2.13}$$

where $\lambda_{he}$ is given by the sum of permanent magnets flux linkage $\Lambda_m$ and excitation flux linkage $M_e I_e$. In this case, limit describes elliptical trajectories in the $d$-$q$ current plane such ellipses have eccentricity equal to the saliency ratio $\xi = \frac{L_q}{L_d}$. Moreover, the ellipses are centered in:

$$\left(-\frac{\Lambda_m + M_e i_e}{L_d}, 0\right) \tag{2.14}$$

where the ratio between the flux linkage and direct inductance is equal to the magnitude of the steady-state three-phase short-circuit current. As the motor speed $\omega_m$ increases, the ellipses become smaller.

Torque limit is obtained from (2.10) , describing trajectories as hyperbola, whose asymptotes are the $d$-axis and the vertical straight line defined by the equation:

$$I_d = -\frac{\lambda_{he}}{(L_d - L_q)}$$

Considering all limits equations, a diagram displaying the limits can be drawn:

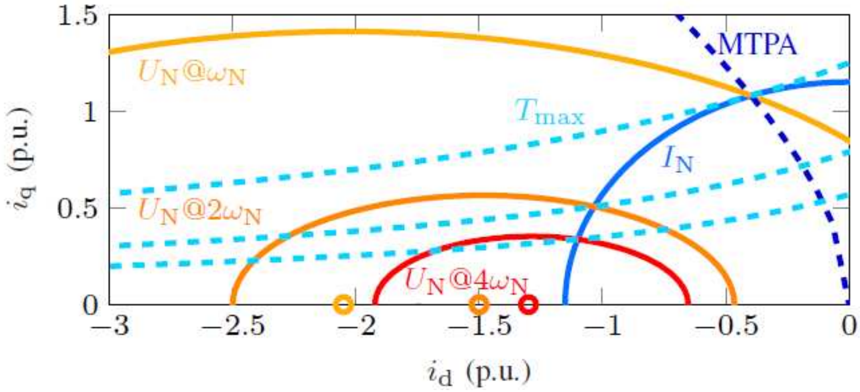

Figure 2.3: HEPM motor limits diagram (considering p.u. values of d-q currents).[11]

To better understand how much excitation is influencing limits, current, voltage and torque limits for PM motor are considered:

$$I_N^2 = I_d^2 + I_q^2 \tag{2.15}$$

$$V_N^2 = R_s^2(I_d^2 + I_q^2) + \omega_{me}^2[(\lambda_m + L_d i_d)^2 + (L_q I_q)^2] \tag{2.16}$$

$$T = \frac{3}{2}p[\Lambda_m + (L_d - L_q)i_d]i_q \tag{2.17}$$

From this, the following diagram can be drawn:

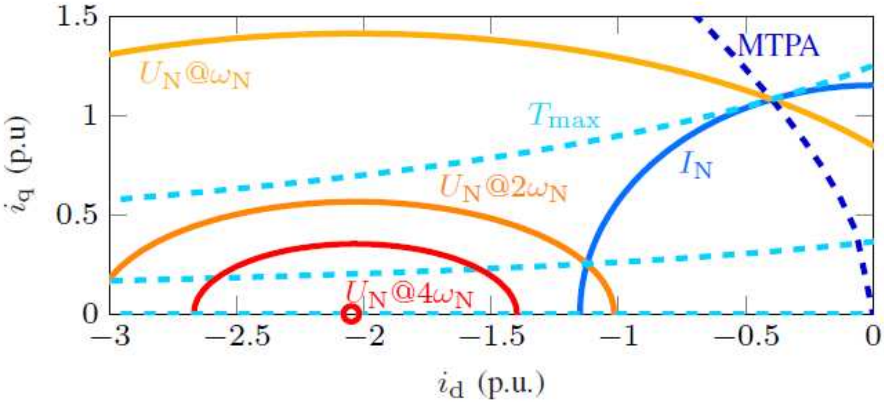

Figure 2.4: PM motor limits digram (considerng p.u. values of d-q currents).[11]

where current, voltage and torque limits are described by circles, ellipses and hyperbolas also in this case, with the difference that for PM there are no excitation contributions. Flux linkage is only due to PMs and, for this, the center of the ellipses is:

$$\left(-\frac{\Lambda_{pm}}{L_d}, 0\right) \tag{2.18}$$

Reporting current, voltage and torque limits on a diagram as circles, ellipses and hyperbolas, makes the research of operating points of the motor easier since they can be easily spotted on the intersections of the curves. In particular, we can pinpoint two important operating regions: MTPA and Flux Weakening.

### 2.2.3 MTPA

At standstill condition, the only constraint that limits the motor torque capabilities is the current limit circle in (2.11). The voltage ellipse constraint described by (2.13) expands, covering the entire *d*-*q* current plane. Indeed, the ellipse size is inversely proportional to the speed. In this condition, the motor is controlled along the *Maximum Torque Per Ampere (MTPA)* strategy. The MTPA trajectory is obtained as the tangent points between current circles and torque hyperbola. Looking at Fig.2.3, the light blue dotted hyperbolas and blue circle for toque and current show the maximum working point for the MTPA trajectory, represented with a blue dotted line.

To compute this trajectory, a desired torque is given and *d*-*q* currents magnitudes are derived from (2.11):

$$I_d = I_N \cos(\alpha) \tag{2.19}$$

$$I_q = I_N \sin(\alpha) \tag{2.20}$$

Substituting in equ. (2.10), yields:

$$T = \frac{3}{2} p[\lambda_{he} I_N \cos(\alpha) + (L_d - L_q) I_N \cos(\alpha) I_N \sin(\alpha)] \tag{2.21}$$

To find the maximum torque available, (2.21) is derived with respect to the angle $\alpha$ and imposed to zero to find:

$$\cos(\alpha) = \frac{-\lambda_{he} + \sqrt{\lambda_{he}^2 + 8(L_d - L_q)^2 I_N^2}}{4(L_d - L_q) I_N} \tag{2.22}$$

it results $\alpha = 117^{\circ}$. From (2.19) and (2.20) and data from Table 2.1, nominal values of *d*-*q* currents are $I_{dN} = -0.91\ A$ and $I_{qN} = 1.78\ A$. The maximum available torque is computed from (2.10) by substituting nominal currents; the result is $T = 6\ Nm$ and it is the nominal torque of the motor. This torque remains the maximum available until the voltage constraint ellipse, shrinking with the increasing of the speed, crosses the MTPA current locus at the nominal current circle. When the motor reaches a certain speed, called *Base Speed*, is no longer

able to keep the maximum torque, since the voltage ellipse constraint forces the working point to lie on a lower hyperbola, supplying the nominal current. At higher speeds, the motor is working in the Flux Weakening Region.
Base speed is computed considering the voltage limit (2.13) in two cases:

- A first estimation is carried out assuming $R_s \approx 0$: starting from (2.12), substituting the steady state equations (neglecting the derivative and the resistance in (2.1) and (2.2)), the following equation is obtained :

  $$\omega_{me_{base}} = \frac{V_N}{\sqrt{\lambda_d^2 + \lambda_q^2}} \tag{2.23}$$

  where direct and quadrature fluxes can be retrieved from (2.4) and (2.5), considering nominal values (coming from MTPA computation) for the currents. According to motor data in Table 2.1, the result is $\omega_{me_{base}} = 148\, rad/s$ (that is $n_{base} = 709\, rpm$).

- Considering $R_s \neq 0$: starting always from voltage limit, in this case the steady state equations are substituted in (2.12) without neglecting the resistance, obtaining a second order equation:

  $$\omega_{me_{base}}^2 \Lambda_N^2 + 2\omega_{me_{base}} R_s(\lambda_d I_{Nq} - \lambda_q I_{Nd}) + R_s^2 I_N^2 - V_N^2 = 0 \tag{2.24}$$

  where $I_N^2$ results from (2.11) and nominal flux linkage is $\Lambda_N^2 = \lambda_d^2 + \lambda_q^2$ ($d$-$q$ flux linkages can be retrieved from (2.4) and (2.5)). The result is $\omega_{me_{base}} = 125\, rad/s$, that is $n_{base} = 600\, rpm$.

As we can see from the results, base speed is considerably changing from the case where resistance is negligible to the case where resistance is non-zero. In the case under study, looking at motor parameters shown in Table (2.1) and the field of application, stator resistance can not be neglected. So, the MTPA operating region is effective when the motor speed is lower than $600\, rpm$.

### 2.2.4 FLUX WEAKENING

In a PMSM the maximum speed is limited by the maximum voltage. To increase speed even further, *Flux Weakening (FW)* technique is employed. The maximum available torque for a given speed is determined by the intersection of the current limit circle and the voltage limit ellipse. This intersection begins to shift from the base working points along the limit circle towards the point $(I_N, 0)$, while maintaining a constant Volt-Ampere rating. Two main situations can arise:

- the center of the ellipse $(\frac{-\Lambda_{he}}{L_d}, 0)$ is outside the current limit circle since $\Lambda_{he} > L_d I_N$, as shown in Fig.2.5a. In this case, the working point is moving from base conditions, along the current circle, till point $(-I_N, 0)$, where the motor exhibits zero torque. This implies that the current limit circle and the voltage limit ellipse are tangent and a maximum speed, also said *maximum speed*, can be reached:

$$\omega_{max} = \frac{V_N}{\Lambda_{he} - L_d I_N} \tag{2.25}$$

Reached $\omega_{max}$, the motor is not able to work properly due to the lack of intersections between current circles and voltage ellipses (as red ellipse shown in Fig.2.4 ).

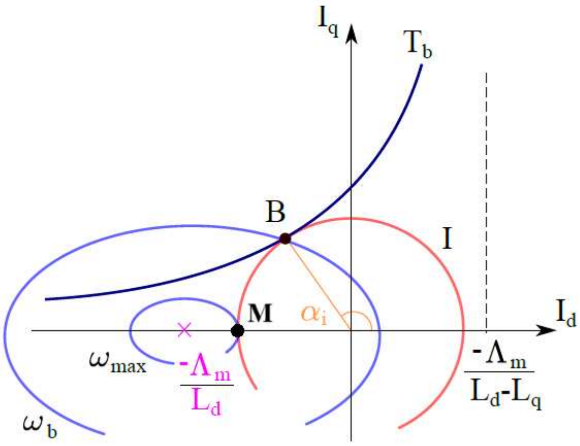

(a) Circle diagram with $\Lambda_{he} > L_d I_N$.

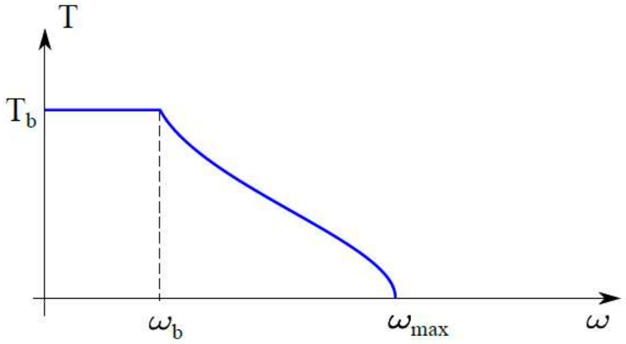

(b) Torque vs. speed diagram with $\Lambda_{he} > L_d I_N$.

Figure 2.5: Circle diagram and torque vs. speed characteristic ($\Lambda_{he} > L_d I_N$).[12]

- the center is placed inside the circle, meaning that $\Lambda_{he} < L_d I_N$, the movement of the current point along the limit circle reaches the point P, shown in Fig.2.6, where the torque hyperbola is tangent to the voltage limit ellipse. At point P, the motor exhibits its maximum torque-to-voltage ratio, and the corresponding electrical speed represents the maximum speed of the FW constant ampere region. Above this speed, the control strategy needs to be adjusted to suite this working condition.

In HEPM motor, the rotor flux $\lambda_{he}$ is variable, the center of the ellipse, in (2.14), is shifted towards the center of the current limit circle, decreasing the excitation winding current. As a result, the maximum speed is theoretically increased up to infinity. Frictions and mechanical issues limit the maximum achievable speed in real world applications.

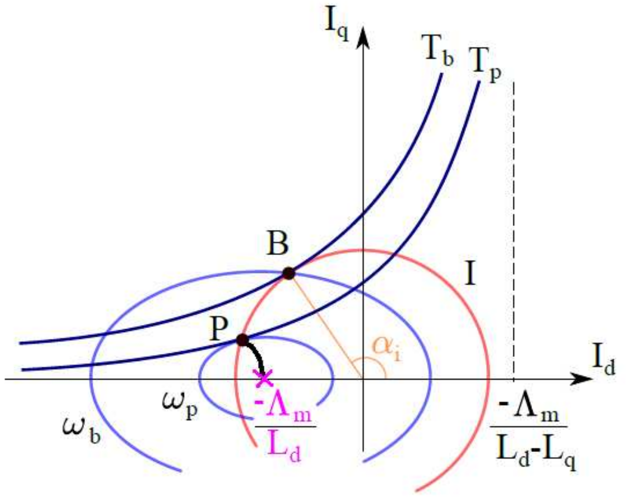

(a) Circle diagram with $\Lambda_{he} < L_d I_N$.

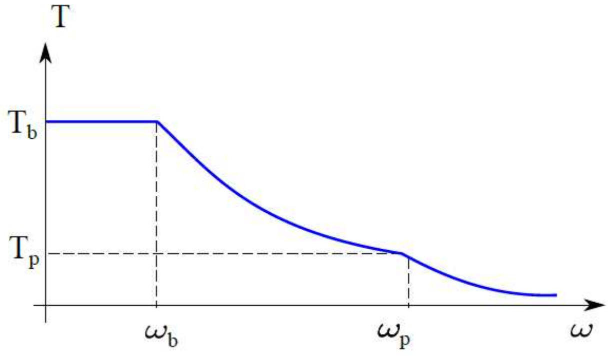

(b) Torque vs. speed diagram with $\Lambda_{he} < L_d I_N$.

Figure 2.6: Circle diagram and torque vs. speed characteristic ($\Lambda_{he} < L_d I_N$).[12]

## 2.3 EXCITATION CONFIGURATION

The presence of excitation windings in HEPM motor poses new challenges: they require a dedicated circuit and a proper current regulation as well as an accurate cooling system. Reaching a compromise between the size of PMs and excitation windings is important to achieve a proper FW performance. Excitation windings give to HEPM machines the opportunity to change the behaviour of the system without acting directly on its geometry.

Rotor flux linkage for HEPM motor is:

$$\lambda_{he} = \Lambda_m + M_e i_e \tag{2.26}$$

where $\Lambda_m$ is the constant component coming from magnets and $\lambda_{de} = M_e i_e$ is the variable component coming from excitation. This two components are following different paths since the HEPM machine under study has a parallel configuration, as shown in Fig. 2.7.

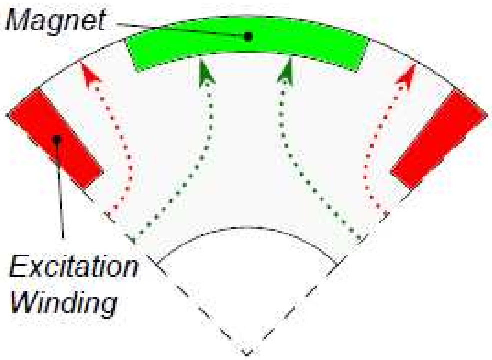

Figure 2.7: Flux linkage paths of the HEPM motor.[9]

In FW region, the center of the ellipse is shifting depending on the excitation flux.

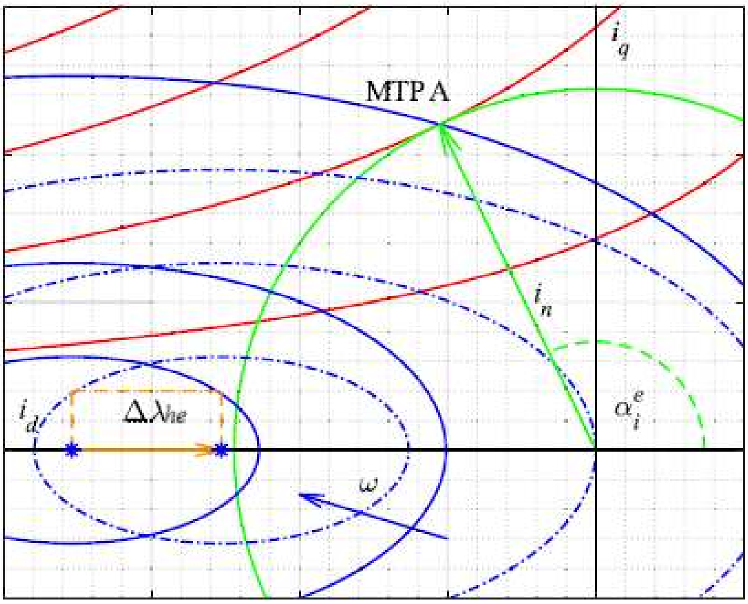

Figure 2.8: Voltage ellipse shifting.[9]

The amount of shifting (in orange in Fig. 2.8), that is the maximum variation of the rotor flux linkage, is:

$$\Delta\lambda_{he} = \lambda_{he,max} - \lambda_{he,min} \tag{2.27}$$

Contribution of PMs and excitation can be arranged in different ways:

1. nominal rotor flux is produced only by PMs and the excitation winding is supplied only to reduce that flux during FW operations. This solution is suitable for motors operating mainly close to the nominal working point and barely on FW conditions.

2. PMs produce the minimum rotor flux $\lambda_{he,min}$ that is required to reach the maximum speed. The excitation winding has to be able to guarantee the difference flux and to obtain the total rotor flux needed in nominal conditions. This solution is suitable for motors often operating at speed higher than the nominal speed, since the higher rotor currents and losses are at low speeds. It is also a solution that requires a lower volume of PMs.

3. excitation winding increases the PM flux at lower speeds and decreases it at high speeds. In this way the maximum rotor current is about half than in previous solutions. There is always current inside the rotor winding. This solution is suggested for motors with frequent variations.

Below we can sum up in a table the properties of the three solutions:

| **Rotor Flux Linkage** | **Solution 1** | **Solution 2** | **Solution 3** |
|---|---|---|---|
| PMs | $\Lambda_m$ | $\Lambda_m$ | $\Lambda_m$ |
| Ex. Winging | $0 \hookrightarrow -\Delta\lambda_{he}$ | $\Delta\lambda_{he} \hookrightarrow 0$ | $\frac{\Delta\lambda_{he}}{2} \hookrightarrow -\frac{\Delta\lambda_{he}}{2}$ |
| $\lambda_{he,max}$ | $\Lambda_m$ | $\Lambda_m + \Delta\lambda_{he}$ | $\Lambda_m + \frac{\Delta\lambda_{he}}{2}$ |
| $\lambda_{he,min}$ | $\Lambda_m - \Delta\lambda_{he}$ | $\Lambda_m$ | $\Lambda_m - \frac{\Delta\lambda_{he}}{2}$ |

Table 2.2: Possible combination of PMs flux and Excitation flux to get $\lambda_{he,max}$.

The third solution is implemented in the HEPM machine under study. During MTPA conditions, excitation flux is constant from zero speed to nominal one. After nominal speed, the motor is in FW and excitation flux is changing according to speed. More in detail, the excitation winding give both a positive and a negative contribution to the rotor flux, by means of the excitation current. The contribution is positive for speeds lower than $\omega_c$, so that the excitation winding increases the flux due to the PMs yielding the nominal rotor flux. At speed higher than $\omega_c$, the excitation winding contribution reduces down to 0 and then it is opposed to the PMs flux, to the aim of decreasing the total rotor flux.
So, accordingly to nominal condition of the excitation current, we compute:

$$\lambda_{he,max} = \Lambda_m + M_e I_{eN} \tag{2.28}$$

$$\lambda_{he,min} = \Lambda_m + M_e(-I_{eN}) \tag{2.29}$$

$$\Delta\lambda_{he} = \lambda_{he,max} - \lambda_{he,min} = 2M_e I_{eN} \tag{2.30}$$

where $\lambda_{he,max} = -\lambda_{he,min} = 0.1789\ Vs$.

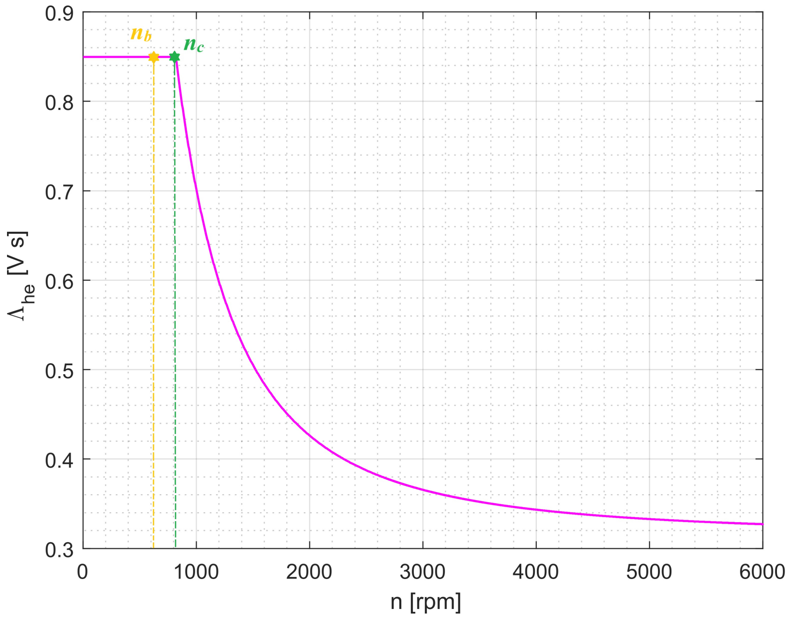

Figure 2.9: Rotor flux linkages as a function of the various electrical speeds.

### 2.3.1 Optimal Rotor Flux Linkage

Rotor flux linkage changes according to speed. In particular, a way to find $\lambda_{he}$ to maximize the torque during FW for any given speed is the *Research of the Optimal Flux Linkage*.
To find the suitable $\lambda_{he}$, $d$-axis and $q$-axis currents are expressed as function of $\lambda_{he}$ using current limit (2.11) and voltage limit (2.13) . Then, substituting the obtained currents in (2.10), the torque becomes a single variable function $T(\lambda_{he})$. Its maximum is found posing its derivative $\frac{dT}{d\lambda_{he}}$ equal to zero.
From this, the optimal flux linkage is:

$$\lambda_{he} = \frac{V_N^2 + \xi(L_d I_N \omega_{fw})^2}{\omega_{fw}\sqrt{V_N^2 + (\xi L_d I_N \omega_{fw})^2}} \tag{2.31}$$

It is a function of the motor parameters $L_d$ and $\xi$, the nominal voltage $V_N$ and current $I_N$ and $\omega_{fw} > \omega_{base}$. Rotor flux linkage behaviour can be shown in Fig.2.9: rotor flux is constant and equal to the nominal value until critical speed; above this speed, rotor flux starts to decrease as in (2.31).

Critical speed is the speed at which rotor flux linkage starts to decrease. The computation of $\omega_c$ with variable rotor flux is obtained reversing (2.31), imposing $\lambda_{he} = \lambda_{he,max}$, yielding:

$$\omega_c = \frac{\sqrt{2}}{\lambda_{he,max}^2 - 2\xi(L_d I_N)^2 + \lambda_{he,max}\sqrt{4\xi^2(L_d I_N)^2 - 4\xi(L_d I_N)^2 + \lambda_{he,max}^2}} \tag{2.32}$$

In the HEPM motor under study, $\omega_c = 138\ rad/s$.

The computation of current phase angle $\alpha_i^e$ depends on the variation of $\lambda_{he}$ and speed $\omega_{fw}$ during FW. At first, the voltage constraint is written as:

$$V_N^2 = \omega_{fw}^2[(\lambda_{he} + L_d I_N \cos\alpha_i^e)^2 + (L_q I_N \sin\alpha_i^e)^2] \tag{2.33}$$

where the only unknown is $\alpha_i^e$. Thus, it is:

$$\cos(\alpha_i^e) = \frac{-\lambda_{he}L_d + \sqrt{\lambda_{he}^2 L_q^2 + (L_d^2 - L_q^2)(\frac{V_N^2}{\omega_{fw}^2} - L_q^2 I_N^2)}}{(L_d^2 - L_q^2)I_N} \tag{2.34}$$

# 3

# HEPM Motor Modeling

In this chapter the HEPM motor model is presented. Also a detailed examination of a control strategy is provided, with each component of the loop dissected. Special emphasis is given to the FW control strategy.

## 3.1 HEPM LINEAR MODEL

The first model described is the linear one. It is built taking into account (2.1),(2.2) and (2.3) written in Laplace domain. Then, considering flux linkages, currents can be recovered from the voltages equations. The procedure is shown in details, starting from (2.1):

$$v_d = R_s i_d + s\lambda_d - \omega_{me}\lambda_q \tag{3.1}$$

where the $d$-axis flux linkage can be written as:

$$\lambda_d = \frac{1}{s}(v_d - R_s i_d + \omega_{me}\lambda_q)$$

remembering that $d$-flux linkage is obtained also as (2.4), $d$-axis current is retrieved:

$$i_d = \frac{\frac{1}{s}(v_d - R_s i_d + \omega_{me}\lambda_q) - \Lambda_m - M_e i_e}{L_d}$$

By doing the same for $q$-axis:

$$v_q = R_s i_q + s\lambda_q + \omega_{me}\lambda_d \tag{3.2}$$

$$\lambda_q = \frac{1}{s}(v_q - R_s i_q - \omega_{me}\lambda_d)$$

with $\lambda_q$ as in (2.5):

$$i_q = \frac{\frac{1}{s}(v_q - R_s i_q - \omega_{me}\lambda_d)}{L_q}$$

For excitation current:

$$v_e = R_e i_e + s\lambda_e \tag{3.3}$$

$$\lambda_e = \frac{1}{s}(v_e - R_e i_e)$$

with (2.6):

$$i_e = \frac{\frac{1}{s}(v_e - R_e i_e) - \frac{3}{2}M_e i_d}{L_e}$$

The mechanical part of the motor, i.e. torque model, can be built considering equation:

$$\tau = \frac{3}{2}p(\lambda_d i_q - \lambda_q i_d) \tag{3.4}$$

From current equations and torque equation, using MATLAB Simulink tool, block schemes can be built. From 3.4 block scheme (3.1) is obtained:

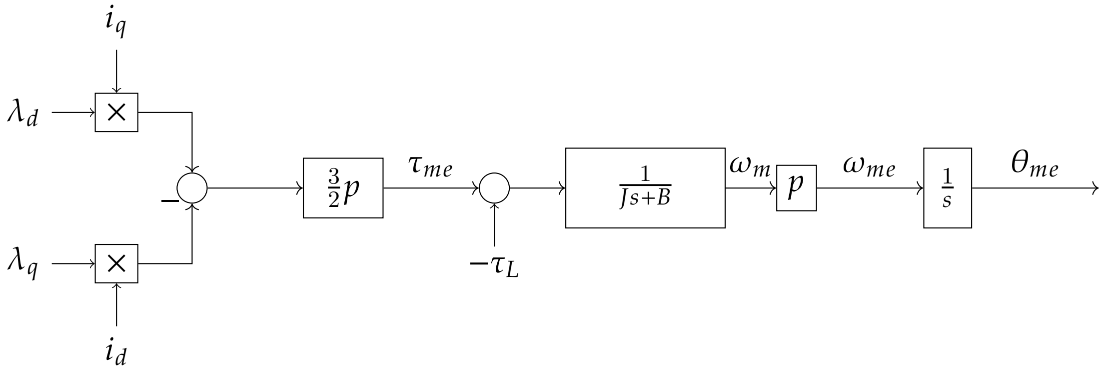

Figure 3.1: Torque model block scheme.

While the electrical block scheme (3.2) , considering the current equations, is:

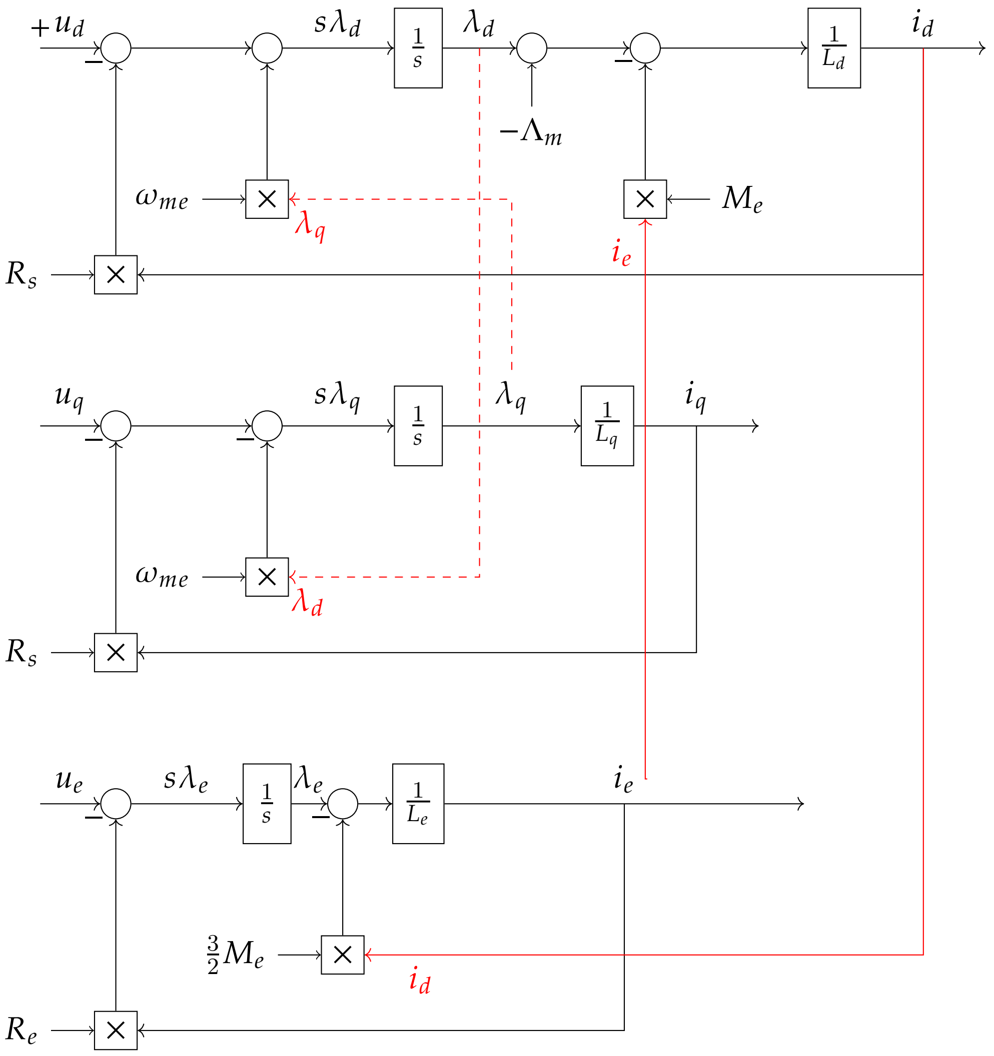

Figure 3.2: Current model block scheme.

## 3.2 HEPM NON-LINEAR MODEL

Flux linkage maps, obtained through *Finite Element Analysis (FEA)*, are highly non-linear and heavily influenced by the rotor excitation current. Non-linearities are due to iron saturation and cross-magnetic effects. In order to accurately replicate the overall motor behavior in a simulation environment, a dynamic model of the HEPM machine is mandatory.

### 3.2.1 NON-LINEAR EQUATIONS

The set of equations related to the non-linear model is more complex with respect to the set used for the linear one. The dynamic voltage balance model of the HEPM motor results:

$$\frac{d\lambda_d(i_d, i_q, i_e)}{dt} = u_d - R_s i_d - \omega_{me}\lambda_q(i_d, i_q, i_e) \tag{3.5}$$

$$\frac{d\lambda_q(i_d, i_q, i_e)}{dt} = u_q - R_s i_q + \omega_{me}\lambda_d(i_d, i_q, i_e) \tag{3.6}$$

$$\frac{d\lambda_e(i_d, i_q, i_e)}{dt} = u_e - R_e i_e \tag{3.7}$$

where $u_d$, $u_q$ and $i_d$, $i_q$ are the $d$-$q$ stator voltage and current components, $u_e$ and $i_e$ are the rotor excitation voltage and current, respectively. $R_s$ and $R_e$ represent the stator and rotor windings resistances, while $\omega_{me}$ is the angular electric frequency. Finally, $\lambda_d(\cdot)$, $\lambda_q(\cdot)$ and $\lambda_e(\cdot)$ are the stator and rotor flux linkages, which all depends on the operating current set-point. The set of equations can be condensed in the following compact matrix expression:

$$\frac{d\boldsymbol{\lambda}(\boldsymbol{i})}{dt} = \boldsymbol{u} - \boldsymbol{R}\boldsymbol{i}(\boldsymbol{\lambda}) - \omega_{me}\boldsymbol{J}\boldsymbol{\lambda}(\boldsymbol{i}) \tag{3.8}$$

being $\boldsymbol{u} = [u_d, u_q, u_e]^T, \boldsymbol{\lambda} = [\lambda_d, \lambda_q, \lambda_e]^T, \boldsymbol{i} = [i_d, i_q, i_e]^T$ ,

$$\boldsymbol{R} = \begin{bmatrix} R_s & 0 & 0 \\ 0 & R_s & 0 \\ 0 & 0 & R_s \end{bmatrix}$$

, and

$$\boldsymbol{J} = \begin{bmatrix} 0 & 1 & 0 \\ -1 & 0 & 0 \\ 0 & 0 & 0 \end{bmatrix}$$

It is worth highlighting the explicit dependency of flux linkages $\boldsymbol{\lambda}(\boldsymbol{i})$ and currents $\boldsymbol{i}(\boldsymbol{\lambda})$.

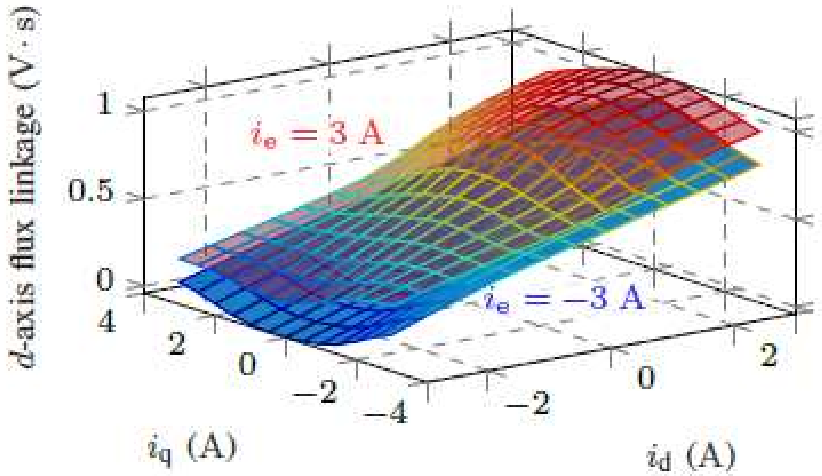

(a) *d*-axis flux linkage.

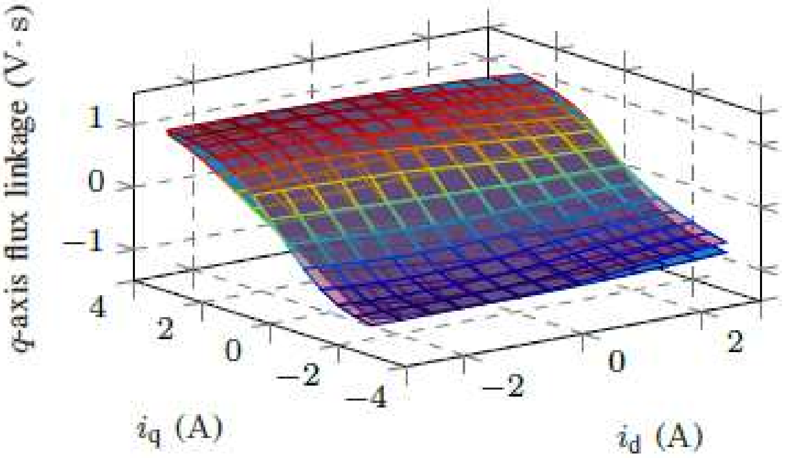

(b) *q*-axis flux linkage.

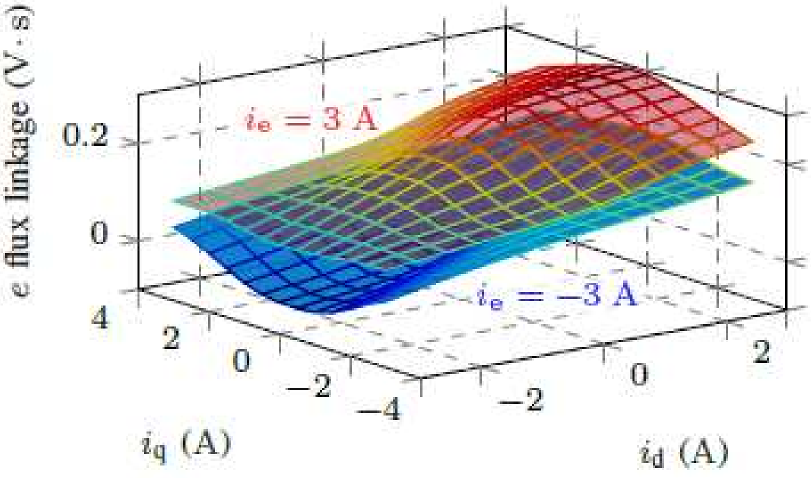

(c) *e* flux linkage.

Figure 3.3: HEPM motor current-to-flux linkage characteristics for the minimum and maximum rotor excitation current $i_e$.[13]

In Fig.3.3, the current-to-flux linkage characteristics of a HEPM motor are shown. They are obtained through FEA. The flux-linkage surfaces are computed for the minimum and maximum excitation current values $i_e = -3A$ and $i_e = 3A$ respectively. These maps are generated according to this procedure: a current set-point $\boldsymbol{i} = [i_d, i_q, i_e]^T$ is mapped in the $d$-axis flux linkage set point $\lambda_d(i_d, i_q, i_e)$ lying in the volume between the two surfaces depicted in the figure, with $\sqrt{i_d^2 + i_q^2} \leq I_N$ and $\| i_e \| \leq I_{eN}$, where $I_N$ and $I_{eN}$ are the stator and rotor rated current values, respectively. A closer look to the curves reveals that the cross magnetic coupling is not negligible both between the $d$ and $q$-axis. Moreover, concerning the $\lambda_e$ map, the effect of $i_e$ is strongly nonlinear. Indeed, $i_e$ does not simply increase $\lambda_e$, but it significantly changes the shape of the flux surfaces too. As a further remark, considering the low reluctance axis ($q$-axis), the iron saturation effect on the $\lambda_q$ characteristic is relevant, leading to non planar surfaces.
So, reproducing the HEPM motor electrical behavior means solving the *Ordinary Differential Equation (ODE)* (3.8) in a simulation environment. Since currents and flux-linkages appear on both sides, the equation solution is not trivial. For this reason, flux-based and current-based models are employed. These two type of models are the dual of each other and both need as input the current-to-flux characteristics $\boldsymbol{\lambda}(\boldsymbol{i})$.

### 3.2.2 Flux-based description

A flux-linkage based model for HEPM motor can be implemented in a simulation environment by solving (3.8). The resulting control scheme is reported in Fig. 3.4:

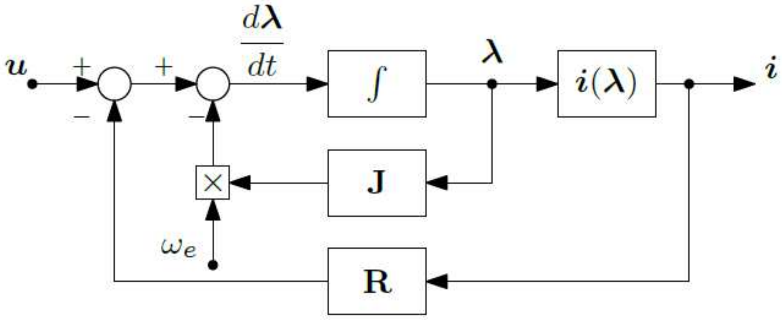

Figure 3.4: Flux-linkage model of a HEPM motor.[13]

The ODE model (3.8) is solved adopting the flux-linkage as unknown while the motor currents are retrieved considering a static nonlinear 3D map $\boldsymbol{i}(\boldsymbol{\lambda})$. Even if only one non-linear map is required, the $\boldsymbol{i}(\boldsymbol{\lambda})$ map is hard to compute. Maps computed during FEA describe the current-to-flux linkage $\boldsymbol{\lambda}(\boldsymbol{i})$ characteristics, therefore, to obtain the flux-to-current maps, an inversion operation is required. Inverting the maps is not easy because of the difficulty of calculationg the domain in which the invertion has to computed, due to the particular shape of the maps [13].

### 3.2.3 CURRENT-BASED DESCRIPTION

The current-based representation of HEPM motors is obtained by applying the chain rule to (3.8) and by substituting the flux linkages with a function of the motor currents:

$$\frac{d\boldsymbol{\lambda}(\boldsymbol{i})}{d(\boldsymbol{i})}\frac{d(\boldsymbol{i})}{dt} = \boldsymbol{L}(\boldsymbol{i})\frac{d(\boldsymbol{i})}{dt} = \boldsymbol{u} - \boldsymbol{R}\boldsymbol{i} - \omega_{me}\boldsymbol{J}\boldsymbol{\lambda}(\boldsymbol{i}) \tag{3.9}$$

where $\boldsymbol{L}(\boldsymbol{i})$ is the incremental inductance matrix, i.e. the Jacobian matrix containing the gradient of the flux-linkage curves with respect to the motor currents:

$$\boldsymbol{L}(\boldsymbol{i}) = \begin{bmatrix} l_{dd} = \frac{\delta\lambda_d}{\delta i_d} & l_{dq} = \frac{\delta\lambda_d}{\delta i_q} & l_{de} = \frac{\delta\lambda_d}{\delta i_e} \\ l_{qd} = \frac{\delta\lambda_q}{\delta i_d} & l_{qq} = \frac{\delta\lambda_q}{\delta i_q} & l_{qe} = \frac{\delta\lambda_q}{\delta i_e} \\ l_{ed} = \frac{\delta\lambda_e}{\delta i_d} & l_{eq} = \frac{\delta\lambda_e}{\delta i_q} & l_{ee} = \frac{\delta\lambda_e}{\delta i_e} \end{bmatrix} \tag{3.10}$$

Since current-to-flux linkage characteristics are non-linear, all the matrix components depend on the current operating set-point. Such dependence is omitted in the equations to ease the notation. Fig. 3.5 shows the resulting dynamic model. The ODE model (3.9) is solved with respect to the motor currents. Two nonlinear static maps are needed in the solution, i.e. $\boldsymbol{L}(\boldsymbol{i})$ and $\boldsymbol{\lambda}(\boldsymbol{i})$. The main advantage of the current approach is that inverse $\boldsymbol{\lambda}(\boldsymbol{i})$ maps are not required, avoiding all the issues discussed in the previous Section. The inversion of a nonlinear 3D function is replaced by the inversion of the incremental matrix $\boldsymbol{L}(\boldsymbol{i})$ (3.10), which is more affordable since a good and smooth approximation of the incremental inductances is available. The law of conservation of energy eases the computation of $\boldsymbol{L}(\boldsymbol{i})$ matrix, exploiting its reciprocity, as in 3.11:

$$l_{dq} = l_{qd}, \qquad l_{de} = \frac{2}{3}l_{ed}, \qquad l_{qe} = \frac{2}{3}l_{eq} \tag{3.11}$$

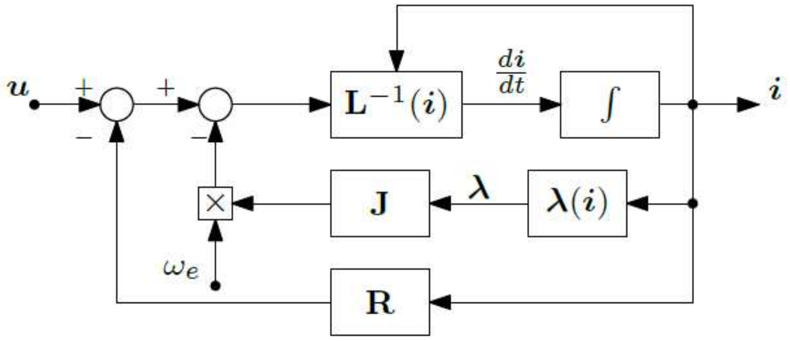

Figure 3.5: Current model of a HEPM motor.[13]

In Fig. 3.6 all these inductances are shown. It is remarkable that both $l_{dq}$ (Fig. 3.6e) and $l_{eq}$ (Fig. 3.6f) share the same order of magnitude with $l_{dq}$ (Fig. 3.6e). However, state-of-the-art of current-based models neglect the effects of the last two inductances, whereas only the former one is always included in the modeling. In other words, only the excitation winding and direct axis coupling is taken into account and $l_{dq} = l_{eq} = 0$ is assumed.
The HEPM motor model is implemented with current-based description and, differently from the state-of-art, the proposed model takes into account all the incremental inductances.

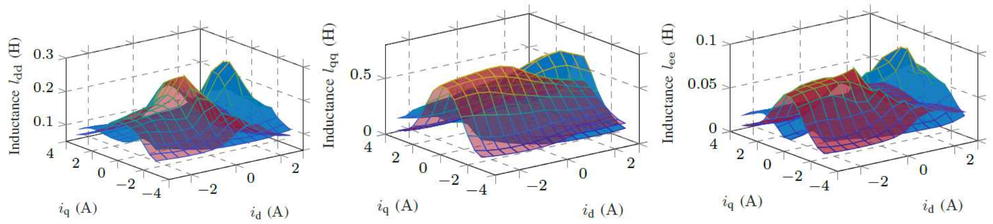

(a) $d$-axis incremental inductance.

(b) $q$-axis incremental inductance.

(c) $e$ incremental inductance.

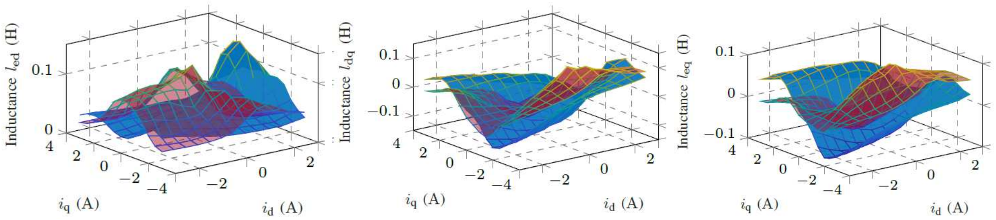

(d) $e$-$d$ cross incremental inductance.

(e) $d$-$q$ cross incremental inductance.

(f) $e$-$q$ cross incremental inductance.

Figure 3.6: Inductances maps (provided for the minimum and maximum $i_e$ values).[13]

## 3.3 Control Scheme

The overall control scheme of HEPM motor is reported in Fig. 3.7 and it is characterized by a conventional cascaded structure.

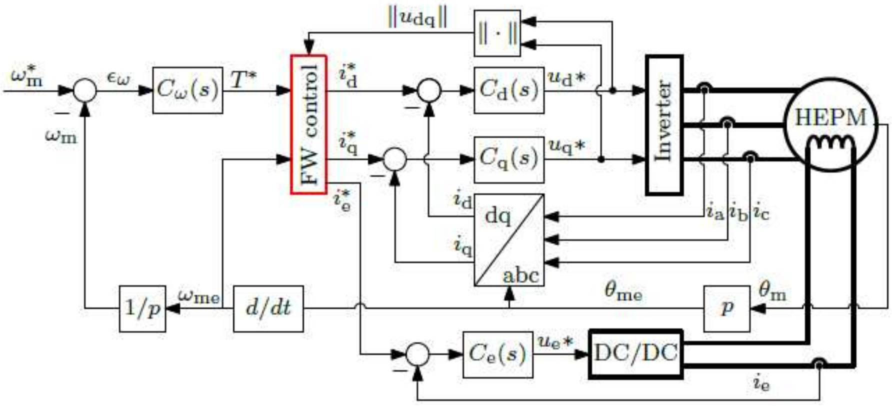

Figure 3.7: Control scheme of an HEPM motor.[11]

Each part of the control is described in details in the following paragraphs.

### 3.3.1 Speed Control

The outer speed loop steers the motor speed $\omega_m$ to the desired reference $\omega_m^*$. The speed regulator $C_\omega(s)$ consists of a conventional PI controller, which zeros the speed reference tracking error $\epsilon_\omega$ and generates the torque reference $T^*$. The block scheme is showed in the following Fig.(3.8):

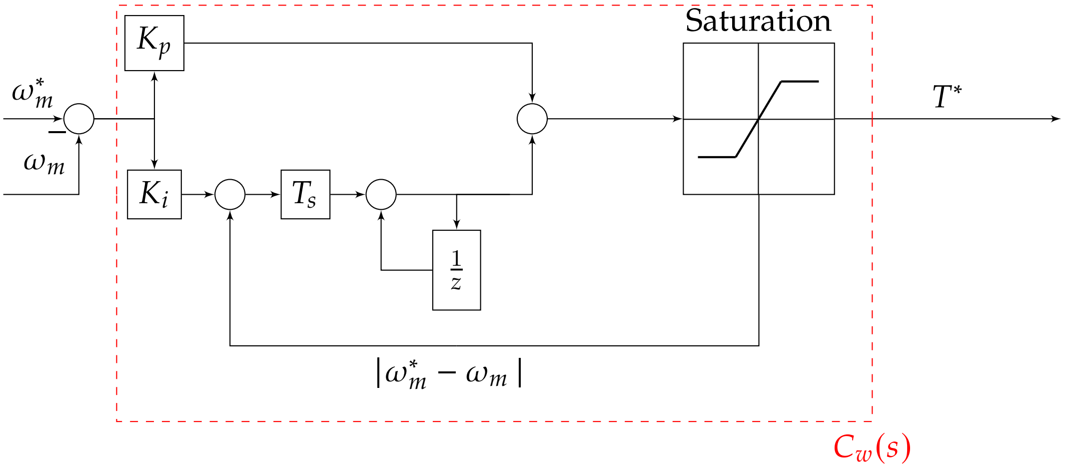

Figure 3.8: Speed control scheme.

Proportional and integral gain are tuned iteratively. A saturation action is present, implementing an anti-windup technique. This is necessary because at some point, due to the integral action, the output can saturate before the error is brought to zero, thereby nullifying the effect of the integral control on the error itself. Thus, anti-windup allows us to terminate the integral action by acting on it through a feedback mechanism as soon as output saturation is reached.

### 3.3.2 CURRENT CONTROL

To control the current, inner loops for $d$-$q$ axis are designed following this procedure: at first, a specific bandwidth ($w_{cc}$) is fixed for the loop and then proportional and integral gains are computed as in (3.12) and (3.13):

$$K_{i(d,q)} = \frac{R}{w_{cc}} \tag{3.12}$$

$$K_{p(d,q)} = \frac{L_{(d,q)}}{R * K_{i(d,q)}} \tag{3.13}$$

The PI control scheme for $d$-$q$ axis are shown in Fig. 3.9 and Fig. 3.10:

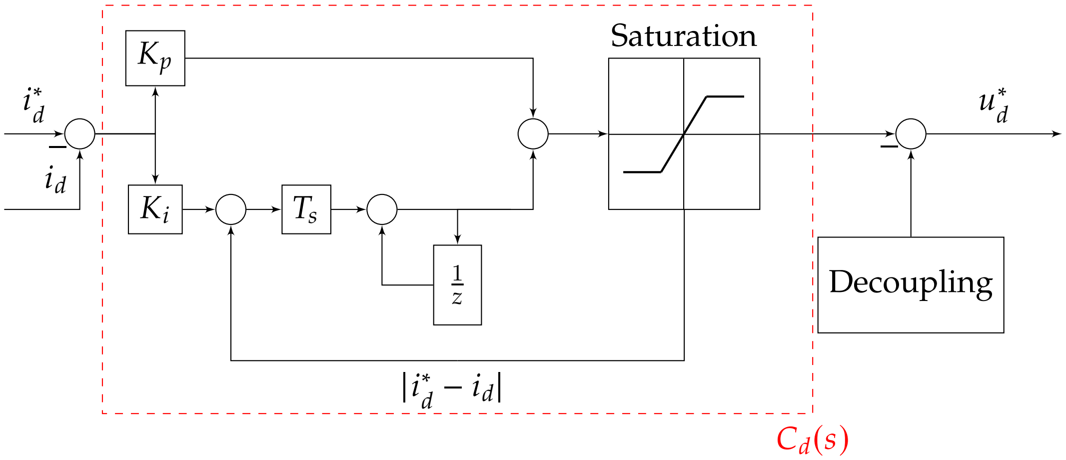

Figure 3.9: d-current control scheme.

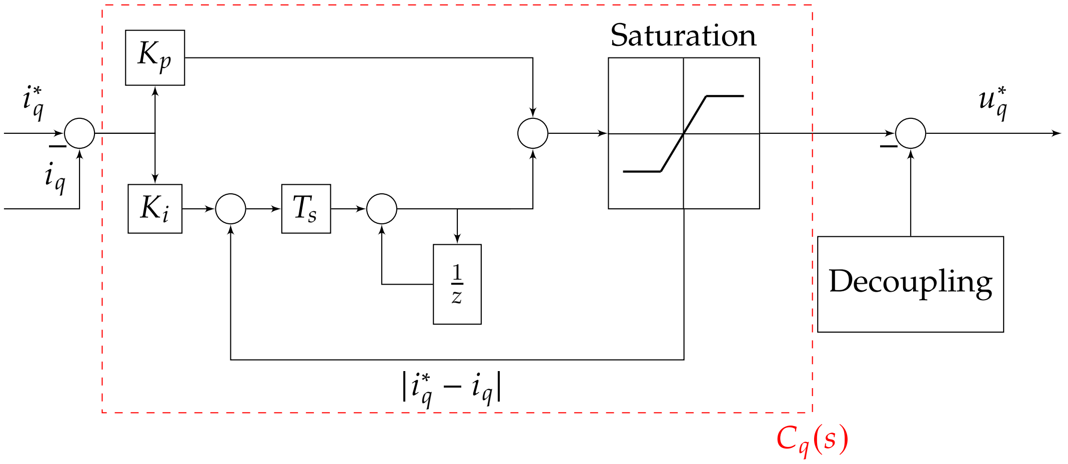

Figure 3.10: q-current control scheme.

Saturation is implemented as in speed loop. Decoupling is needed in this case since $d$ and $q$ axis are coupled. Moreover, the $q$-axis control output is influenced by *Back Electro-Motive Force (BEMF)* so the decoupling strategy has the goal to compensate it as well. $d$-$q$ axis voltages reference computed as output are the inputs for the inverter set to control the motor.

### 3.3.3 FLUX-WEAKENING CONTROL

The FW block represents the core of the proposed control methodology. To implement it there are three ways:

- **FEED-FORWARD SCHEME:** consists of computing the FW $d$-axis current reference by exploiting an accurate analytical model of the motor. Inputs include the torque reference from the speed regulator, the motor speed, and all the electric motor parameters. The main advantages of this method are its simplicity, which is beneficial when dealing with complex models, and its good performance during transients. Additionally, it does not suffer from stability issues, and no parameter tuning is required. However, this method is sensitive to parameter mismatches.
  FW operation is often needed in demanding applications, but sensitivity issues must be addressed. Specifically, to accurately construct the model, maps analyzing the impact of parameter mismatches on the motor can be generated. In cases where the mismatch is not significant, another option is to neglect its effect. In Fig. 3.11 a feed-forward scheme is shown.

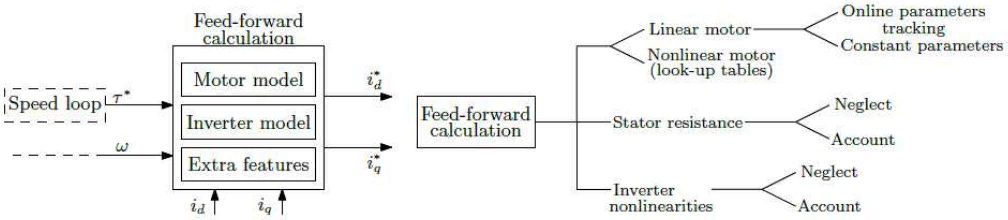

Figure 3.11: Scheme of a standard feed-forward FW control architecture.[12]

- **FEED-BACK SCHEME:** implements feedback on the inverter reference voltages to achieve FW operation. The plant model is not explicitly used by feedback algorithms. However, the electrical model is required for tuning the voltage loop regulator, and accurate model knowledge is mandatory to linearize the loop. The two main advantages of this solution are its parametric robustness and the higher utilization of the available inverter DC-bus voltage. On the downside, the feedback strategy introduces a delay in the dynamic performance of the loop.
  There are two categories of feedback schemes, based on how the loop acts on the current reference from the speed loop. These can be distinguished as follows: one method acts on the MTPA angle of the current references (Fig. 3.12a), while the other acts directly on the $d$-current reference (Fig. 3.12b).

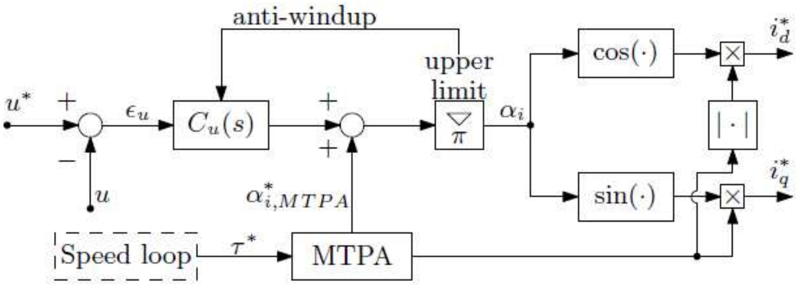

(a) Flux-weakening voltage loop with angle control.

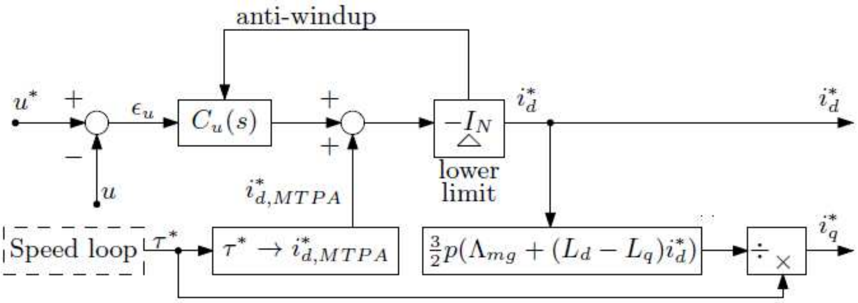

(b) Flux-weakening voltage loop with $d$-current control.

Figure 3.12: Feedback FW control architecture.[12]

The dynamic of the current angle is strongly non linear. Moreover linearization of the angle loop requires the computation of a non trivial linearizing gain. From this, the *d*-axis current strategy appears more convenient.

- **HYBRID SCHEME:** incorporates both a voltage control loop and a feed-forward component. The feed-forward contribution is calculated using the motor model. As with feedback structures, the reference d-axis current or current angle is then adjusted according to the output of the voltage loop. This approach enhances the feed-forward action. Hybrid schemes aim to combine the benefits of both structures mentioned earlier, namely, fast dynamics and robustness against parameter variations.

The hybrid strategy is implemented for the HEPM motor under study, featuring a feed-forward excitation current reference generation and a feedback control of the stator voltage magnitude. FW block scheme is reported in Fig. 3.13:

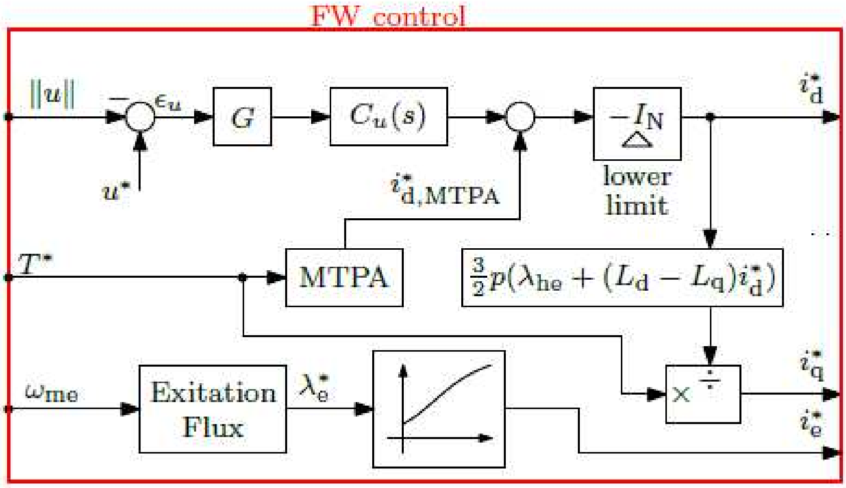

Figure 3.13: Flux-weakening block (detail of Fig. 3.7).[11]

### MTPA.

The computation of the MTPA trajectory is implemented using a *Look Up Table (LUT)* with 1D-spline interpolation (Fig. 3.14). The table is generated by interpolating *d*-current and torque values obtained from measurements. In this way, each torque reference value can be associated with a specific *d*-current set point.

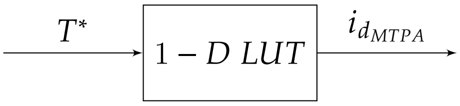

Figure 3.14: MTPA block scheme.

The resulting map is showed in Fig. 3.15.

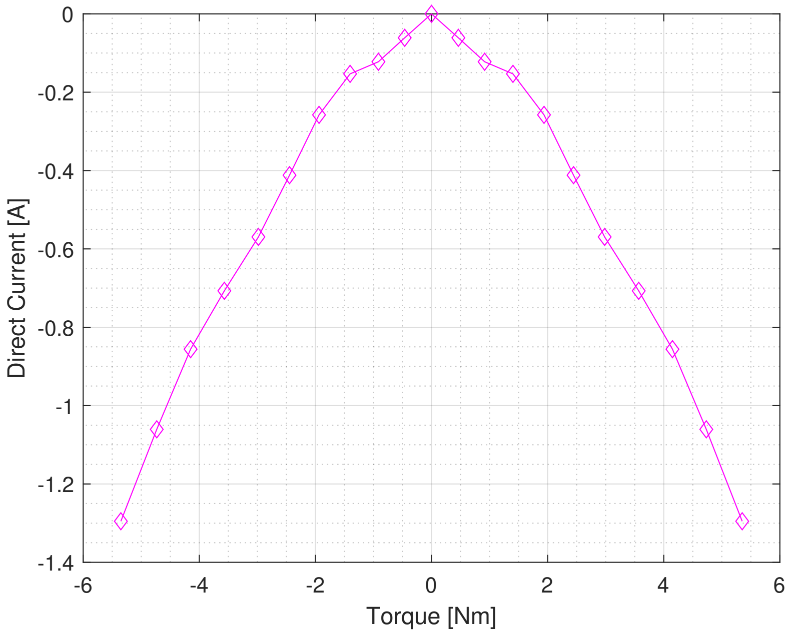

Figure 3.15: MTPA LUT map.

### LINEARIZATION.

The relationship between current and voltage vector magnitude is strongly non-linear. Therefore, the design and tuning of the voltage loop is challenging. To address these challenges, a method to analytically compute the nonlinear gain of the voltage loop and linearize it is implemented. This allows for achieving the desired bandwidth of the voltage loop with more reliability. An overview is hereafter described:

- **Defing Nonlinear Relationship**: The first step is to recognize that the current and voltage relationship is nonlinear. This means that the voltage response to changes in current is not proportional, making it difficult to predict and control.

- **Analytical Computation of Nonlinear Gain:** To compensate for this nonlinearity, the gain of the voltage loop is analytically computed. This involves deriving mathematical expressions that accurately describe how the gain varies with operating conditions.

- **Linearization of the Voltage Loop:** Once the nonlinear gain is known, the next step is to linearize the voltage loop. This is done by designing a compensator or controller that adjusts the gain in real-time, effectively making the overall system behave linearly.

- **Ensuring Desired Bandwidth:** With the voltage loop linearized, standard linear control design techniques can be used to tune the loop. This includes setting the desired bandwidth, which determines how quickly the system can respond to changes. By ensuring the loop has a consistent gain, the desired bandwidth can be achieved more reliably.

Since for the considered HEPM motor $d$-axis flux, the voltage loop is exploited ro adjust the $d$-axis MTPA current reference during FW. The voltage magnitude expression results:

$$\|u\| = \sqrt{u_d^2 + u_q^2} \tag{3.14}$$

Thus, from a small signal perspective, $i_d$ produces nonlinear effects on $\|u\|$, in fact:

$$\begin{aligned}\frac{\partial\|u\|}{\partial i_d} &= \frac{1}{U}\left(U_d\frac{\partial u_d(i_q)}{\partial i_q} + U_q\frac{\partial u_q(i_d)}{\partial i_d}\right)\\ &= \frac{1}{U}\left(U_d\frac{\partial u_d(i_q)}{\partial i_q}\frac{\partial i_q}{\partial i_d} + U_q\frac{\partial u_q(i_d)}{\partial i_d}\right)\end{aligned} \tag{3.15}$$

where lowercase letters stand for the total quantities, while uppercase letters stand for large-signal dc quantities. The nonlinear effect $\frac{\partial\|u\|}{\partial i_d}$ is compensated by including the following linearization gain in the voltage loop:

$$G = \frac{1}{\frac{\partial\|u\|}{\partial i_d}} \tag{3.16}$$

Concerning the computation of the $d$-$q$ voltage partial derivatives, the voltage balance equations (2.7), (2.8) and (2.9) are simplified assuming negligible resistive voltage drops:

$$u_d \approx -\omega_{me}L_q i_q \tag{3.17}$$

$$u_q \approx \omega_{me}(\lambda_m + L_d i_d + M_e i_e(i_d)) \tag{3.18}$$

This assumption is well motivated by the fact that the motional terms are prominent with increasing speed, i.e. in FW operation. Under such hypothesis, the voltage partial derivatives in (3.15) result:

$$\frac{\partial u_d}{\partial i_q} = -\omega_{me}L_q \tag{3.19}$$

$$\frac{\partial u_q}{\partial i_d} = M_e\frac{\partial i_e(i_d)}{\partial i_d}\omega_{me} + L_d \tag{3.20}$$

An additional partial derivative needs to be computed, namely $\frac{\partial i_e}{\partial i_d}$. From a small signal point of view, the effect of a variation of $i_d$ on $i_e$ is derived from the flux model equation (2.6):

$$\frac{\partial i_e}{\partial i_q} = -\frac{3}{2}\frac{M_e}{L_e} \tag{3.21}$$

Concerning the partial derivative $\frac{\partial i_q}{\partial i_d}$, its expression is derived assuming a constant delivered torque. The $q$-current expression for a given torque is obtained from (2.10). Then, substituting (3.16) in the $i_q$ expression, the following equivalence holds:

$$\begin{aligned}\left.\frac{\partial i_q}{\partial i_d}\right|_T &= -\frac{2T\left(L_d - L_q - M_e\frac{\partial i_e}{\partial i_d}\right)}{3p(\lambda_m + M_e I_e + (L_d - L_q)I_d)^2} \\ &= -\frac{I_q(L_d - L_q - \frac{3}{2}\frac{M_e^2}{L_e})}{\lambda_m + M_e I_e + (L_d - L_q)I_d}\end{aligned} \tag{3.22}$$

The nonlinear behavior of the voltage loop can be finally described by substituting (3.19), (3.20) and (3.22) into (3.15):

$$\frac{\partial \|u\|}{\partial i_d} = \frac{\Omega_{me}}{U}\left(U_d\frac{L_q I_q\left(L_d - L_q - \frac{3}{2}\frac{M_e^2}{L_e}\right)}{\lambda_m + M_e I_e + (L_d - L_q)I_d} + U_q\left(L_d - \frac{3}{2}\frac{M_e^2}{L_e}\right)\right) \tag{3.23}$$

Such expression is evaluated each control period to compute the linearizing gain $G$ [14]. The gain computation requires currents and speed measurement, as well as the values of the input voltages applied in the previous control period. In conclusion, compensating for the nonlinear gain in the voltage loop and linearizing it ensures that the desired bandwidth and overall system performance are achieved, despite the inherent nonlinearity in the relationship between current and voltage. This approach enhances the stability and predictability of the control system.

#### VOLTAGE LOOP TUNING.

By applying gain normalization, the nonlinearity of the plant is effectively compensated. This allows the equivalent plant dynamics to be simplified and represented by the transfer function of a closed-loop synchronous current control system. Typically, this system is designed to achieve a first-order low-pass frequency response with the same bandwidth $B_c$ on both synchronous reference frame axes:

$$\frac{I_{d,q}}{I^*_{d,q}}(s) \approx \frac{1}{\left(\frac{1}{2\pi B_c}\right)s + 1} \tag{3.24}$$

This result is simple to analyze. In fact, the expression of the voltage open-loop transefer function becomes:

$$G_{OL} = K_{P_{FW}}\frac{\tau_{PI}s + 1}{\tau_{PI}s}\frac{1}{\left(\frac{1}{2\pi B_c}\right)s + 1} \tag{3.25}$$

making the choice of the gain values for the voltage regulator a simple task, once proper design specifications are given.
A very simple method for tuning the FW regulator consists in applying zero-pole cancellation, using a PI regulator with time constant $\tau_{PI}$ equal to that of the current regulator [14]:

$$\tau_{PI} = \frac{1}{2\pi B_c} = \frac{K_{P_{FW}}}{K_{I_{FW}}} \tag{3.26}$$

After the compensation, in order to achieve the desired closed-loop bandwidth $B_{FW}$, the proportional gain $K_{P_{FW}}$ must be set as follows:

$$K_{P_{FW}} = \frac{B_{FW}}{B_c} \tag{3.27}$$

leading to the following open-loop gain:

$$G_{OL} = K_{P_{FW}} \frac{1}{\tau_{PI} s} = \frac{B_{FW}}{B_c} \frac{1}{\left(\frac{1}{2\pi B_c} s\right)} = \frac{2\pi B_{FW}}{s} \tag{3.28}$$

and the cross-over frequency is the design goal bandwidth. Therefore, the resulting closed-loop response will be:

$$G_{CL} = \frac{U}{U^*} = \frac{1}{\left(\frac{1}{2\pi B_{FW}}\right) s + 1} = \frac{1}{\tau_{FW} s + 1} \tag{3.29}$$

where $\tau_{FW}$ is the time constant of the single pole.

### Voltage loop low pass filters.

To ensure a correct performance of the voltage control during the worst-case transient, low pass filtering is crucial. Filters are designed according to the time constants of the current, speed and voltage regulators, obtaining [15]:

$$\tau_{LPF_{dq}} = \frac{1}{2\pi B_{LPF_{dq}}} \tag{3.30}$$

$$\tau_{LPF_{w}} = \frac{1}{2\pi B_{LPF_{w}}} \tag{3.31}$$

$$\tau_{LPF_{U}} = \frac{1}{2\pi B_{LPF_{U}}} \tag{3.32}$$

The bandwidths $B_{LPF_U}$ and $B_{LPF_{dq}}$ are choosen as an integer multiple of the FW bandwidth, in such a way that $B_{LPF_U} \approx B_{LPF_{dq}}$. In particular, the voltage time constant must be much lower than the FW time constant so that the voltage *Low Pass Filter (LPF)* does not significantly affect the loop response. The speed LPF time constant can be almost equal to that of the control loop.

### 3.3.4 EXCITATION CURRENT CONTROL

The excitation current control aims to maximize the output torque and power of the machine at each operating speed by adjusting the center of the voltage ellipses as needed. From this basis, the optimal rotor flux linkage can be computed, as in (2.31), according to speed variations. Then the current reference is retrived:

$$i_e^* = \frac{1}{M_e}(\lambda_{he} - \lambda_m) \tag{3.33}$$

The current control for excitation is the following:

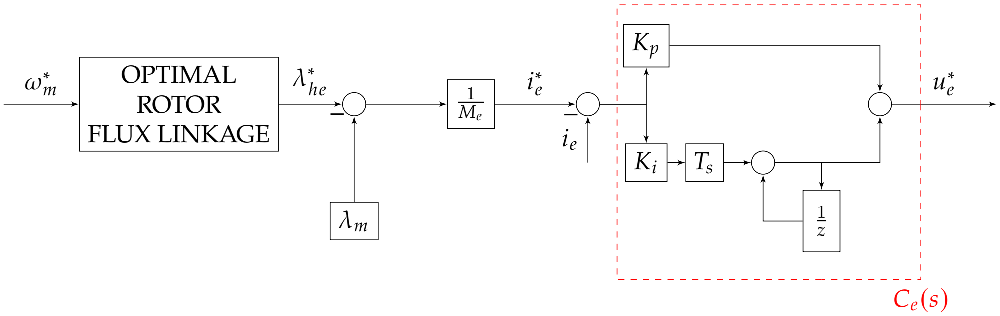

Figure 3.16: Excitation current control scheme.

The proportional and integral gain are tuned iteratively. The output of the PI control scheme gives as output the excitation reference voltage for the DC/DC converter that supplies the excitation winding.

# 4

# MATLAB Simulation Results

In this chapter, the designed control scheme is tested both on the linear and non-linear model using MatLab Simulink. Various speed references are considered to evaluate the model performance in and out FW region. Additionally, the accuracy of the voltage loop is analyzed.

## 4.1 HEPM LINEAR MODEL SIMULATION RESULTS

The first part of the testing process considers the linear model. Two speed references are taken into account: a step reference and a ramp reference.

### 4.1.1 STEP RESPONSE

Fig. 4.1 shows the speed reference and the speed resulting from the simulation. Fig. 4.3 and Fig. 4.4 show, respectively, the direct and quadrature current reference and simulated. Same also for the excitation current in Fig. 4.5. Torque results are shown in Fig. 4.2.

To test the behaviour of the model in every condition, the reference is composed by different speed values. The first step, from $0\ rpm$ to $600\ rpm$, shows the behaviour of the model before reaching the base speed. In this case, $d$-axis current is computed following the MTPA trajectory. With the second step, from $600\ rpm$ to $1200\ rpm$, the motor is working in FW region and excitation current in Fig. 4.5 decreases to reach speeds above the base one. The third step, from $1200\ rpm$ to $2000\ rpm$, shows the behaviour of the linear model at very high speeds, reaching $2000\ rpm$ as limit. Torque in Fig. 4.2, during the changes of the step amplitude, shows overshoots that reach the maximum value of $6\ Nm$. As for the torque, during step changes, overshoots and undershoots are present also in $dq$-axis currents (Fig. 4.3 and Fig. 4.4).

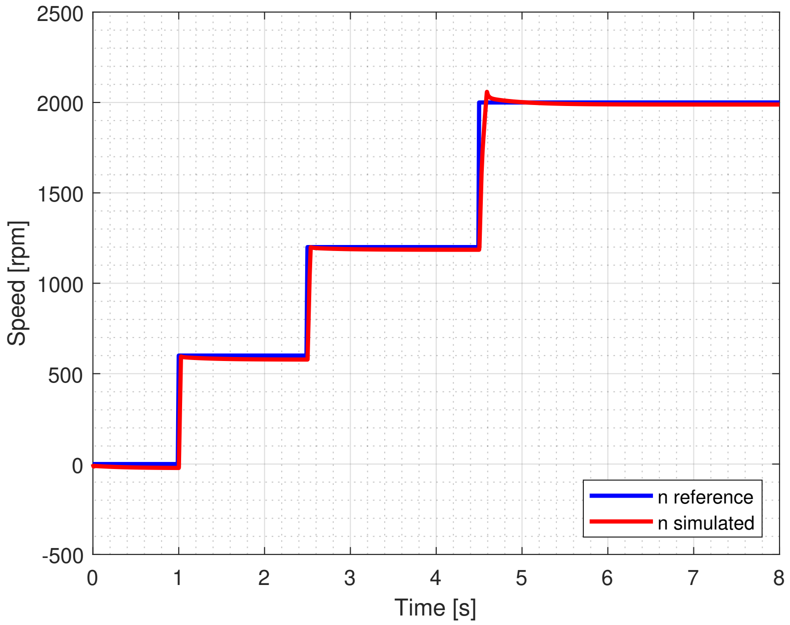

Figure 4.1: Speed.

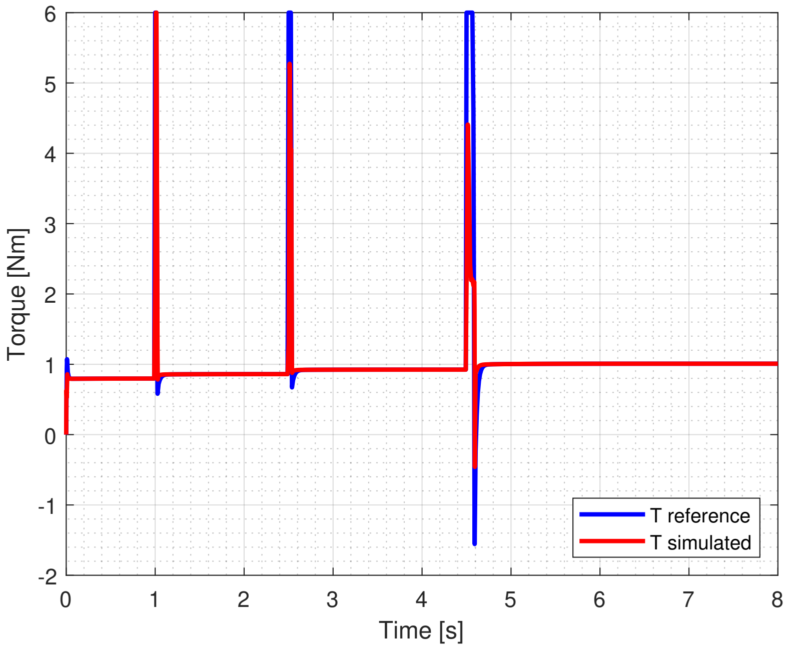

Figure 4.2: Torque.

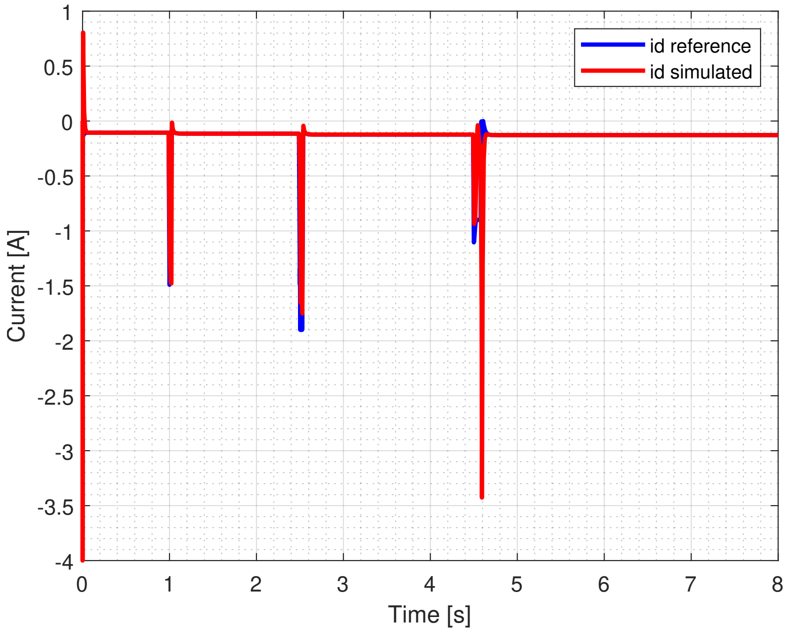

Figure 4.3: *d*-axis current.

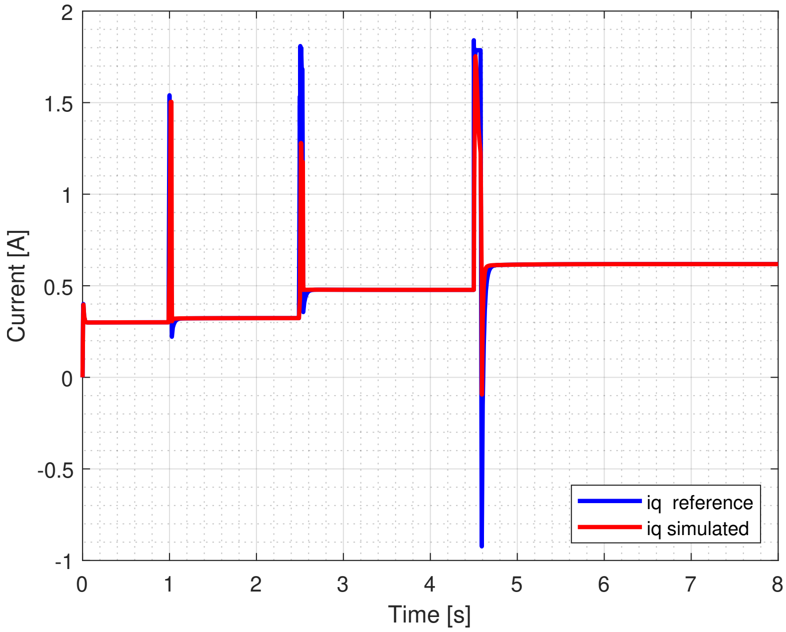

Figure 4.4: *q*-axis current.

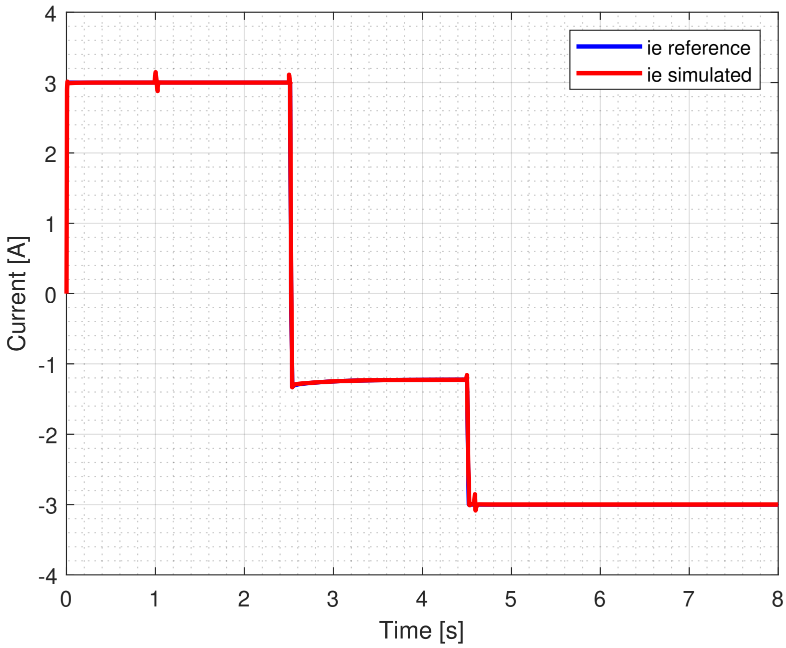

Figure 4.5: Excitation current.

### 4.1.2 Ramp Response

Due to the presence of torque and current overshoots and undershoots, the experimental validation on a real motor could present some problems. For this reason, the step reference is replaced with a reference in which the amplitude is changing gradually. Therefore, the second part of the test is conducted using a speed reference increasing with ramp behaviour, where the slope determined by the ratio between final value and the total simulation time. The resulting ramp is showed in Fig. 4.6 along with the simulation outcome. In Fig. 4.8 and 4.9 there are the resulting $dq$-axis currents:the overshoots and undershoots that previously reached high current values are no longer present with the exception of small spikes at the beginning of the simulation. The same applies to the torque, in Fig. 4.7. The decreasing excitation current, in Fig. 4.10, is more gradual compared to the one in Fig. 4.5.

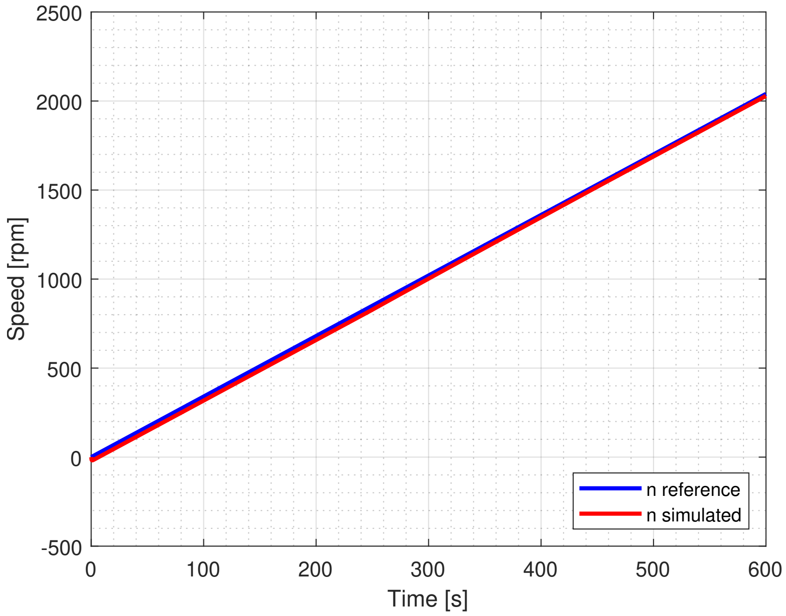

Figure 4.6: Speed.

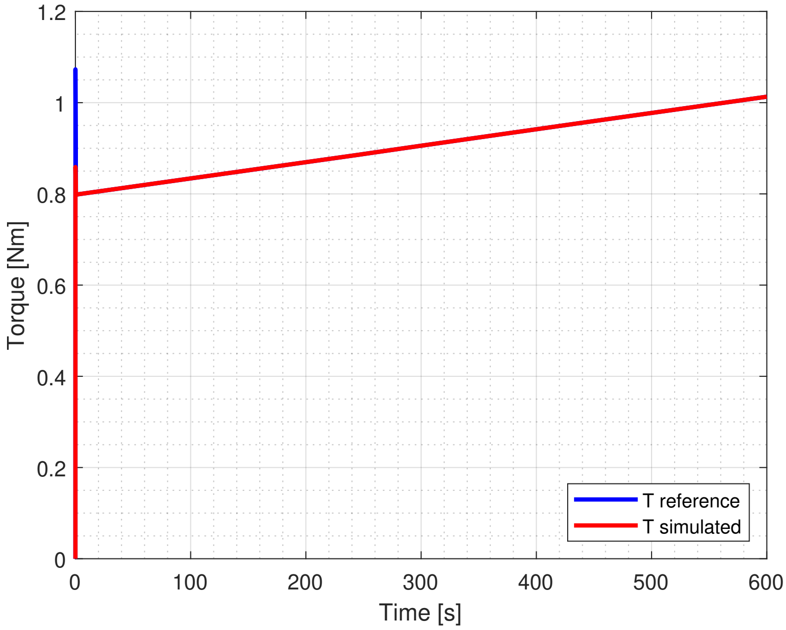

Figure 4.7: Torque.

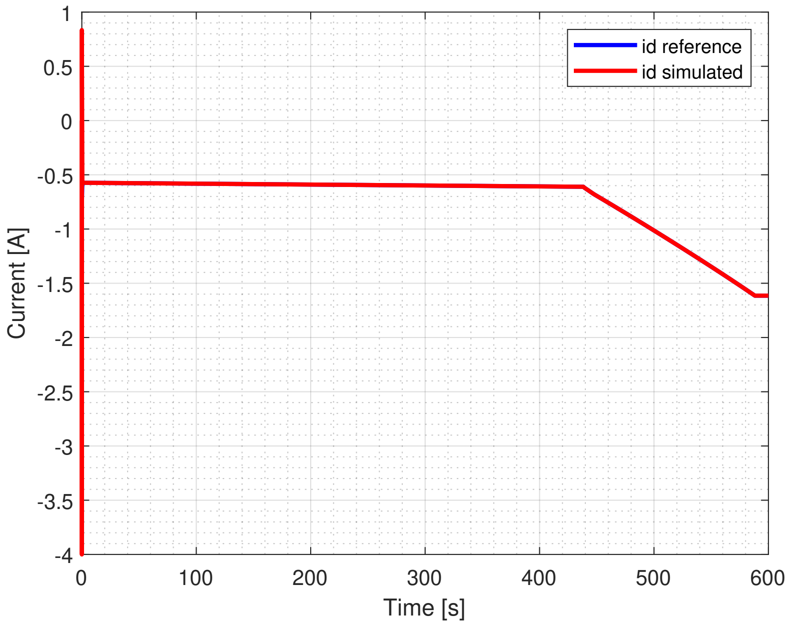

Figure 4.8: *d*-axis current.

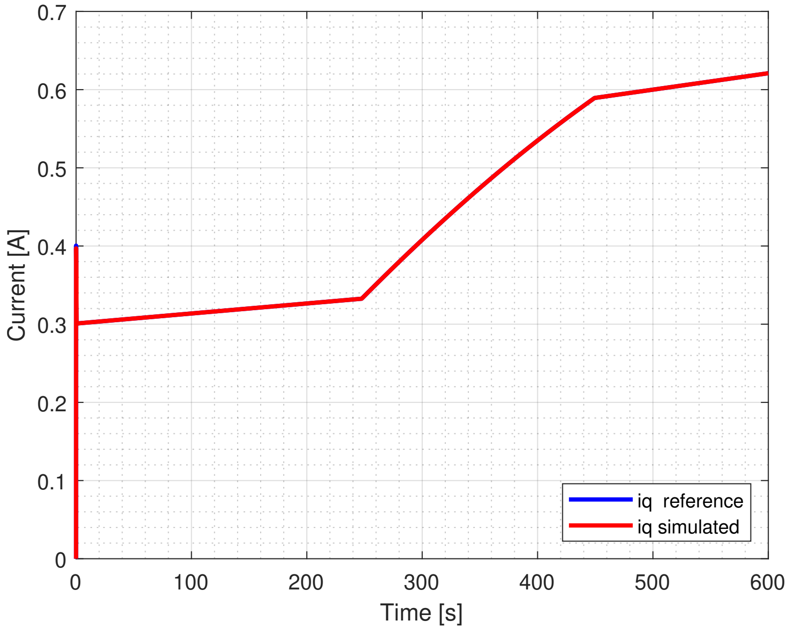

Figure 4.9: *q*-axis current.

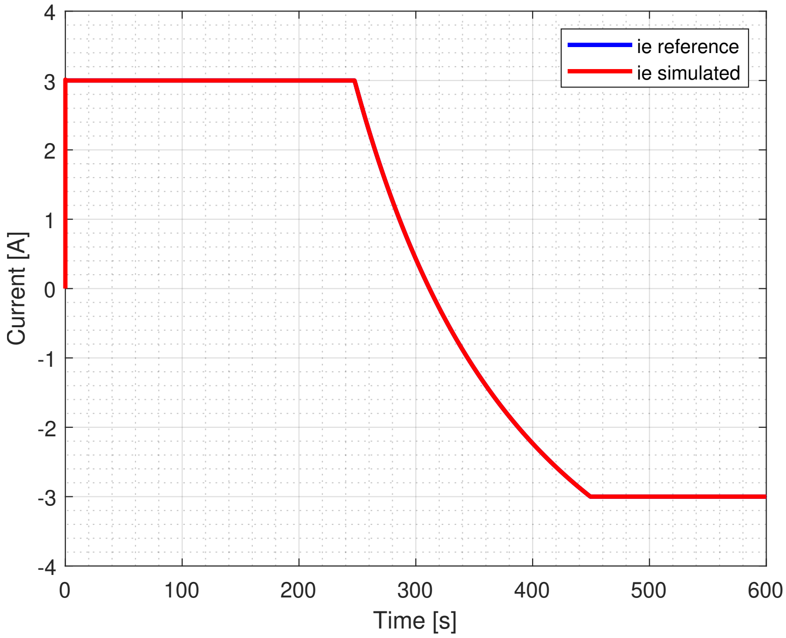

Figure 4.10: Excitation current.

## 4.2 HEPM Non Linear Model Simulation Results

The second part of the test is conducted on the non-linear motor model, testing it under the same conditions as the linear model. Both the step and ramp reference results are analysed.

## 4.3 Step Response

Fig. 4.11 shows the speed reference and the speed resulting from the simulation. Fig. 4.13 and Fig. 4.14 show, respectively, the direct and quadrature current reference and simulated. Same for the excitation current in Fig. 4.15. Torque results are shown in Fig. 4.12.

The model is unable to reach $2000\ rpm$ due to the non linearities of the model, influencing the torque behaviour as well. The torque and currents exhibit undershoots and overshoots during step amplitude changes, which could be problematic when testing a real prototype. Additionally, the torque does not perfectly follow the reference due to the lack of information regarding the excitation current within the MTPA maps. This issue is investigated in detail in Section 4.5.

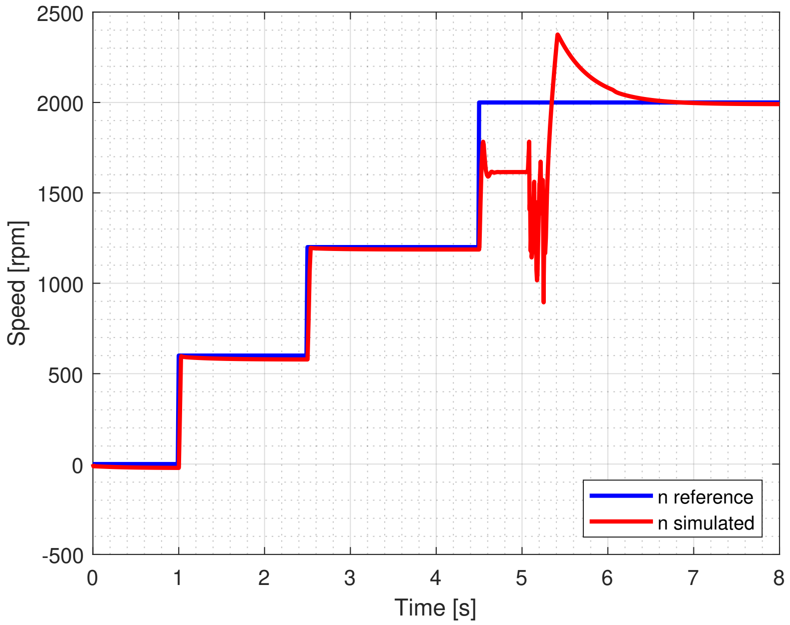

Figure 4.11: Speed.

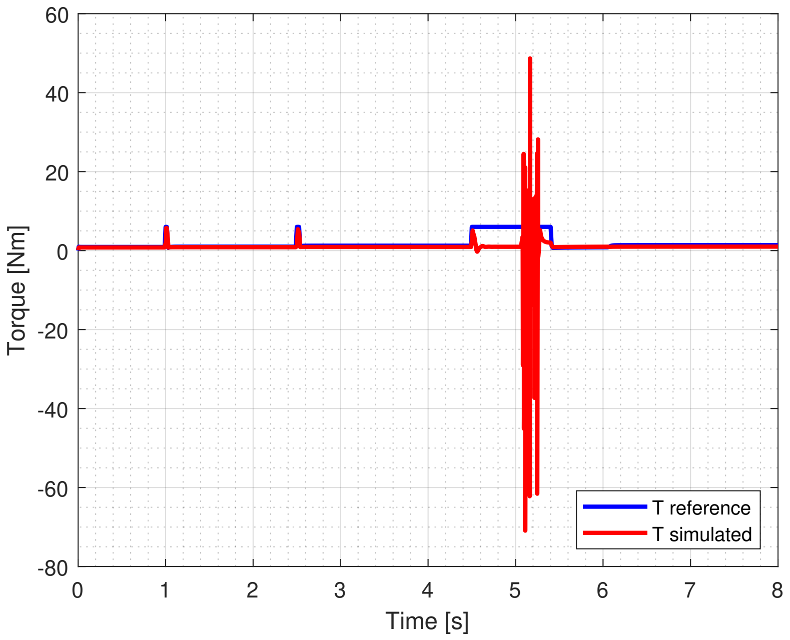

Figure 4.12: Torque.

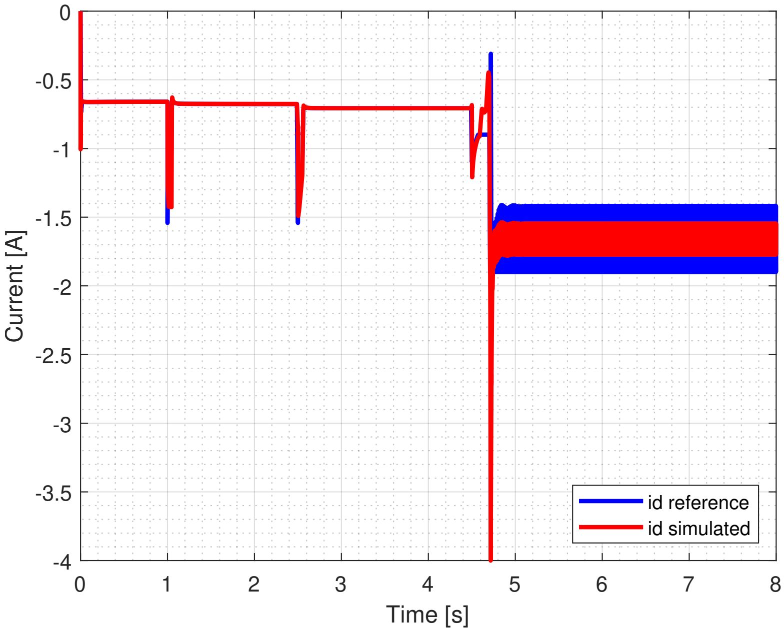

Figure 4.13: $d$-axis current.

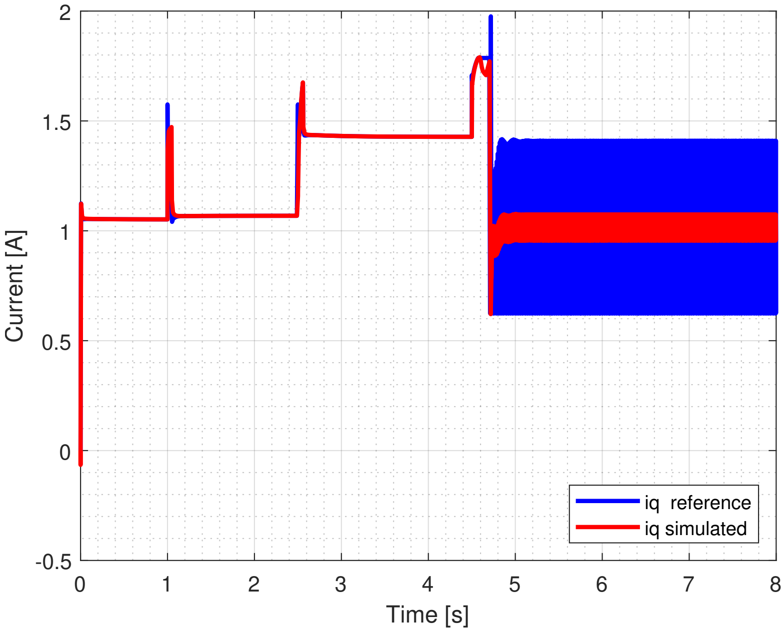

Figure 4.14: $q$-axis current.

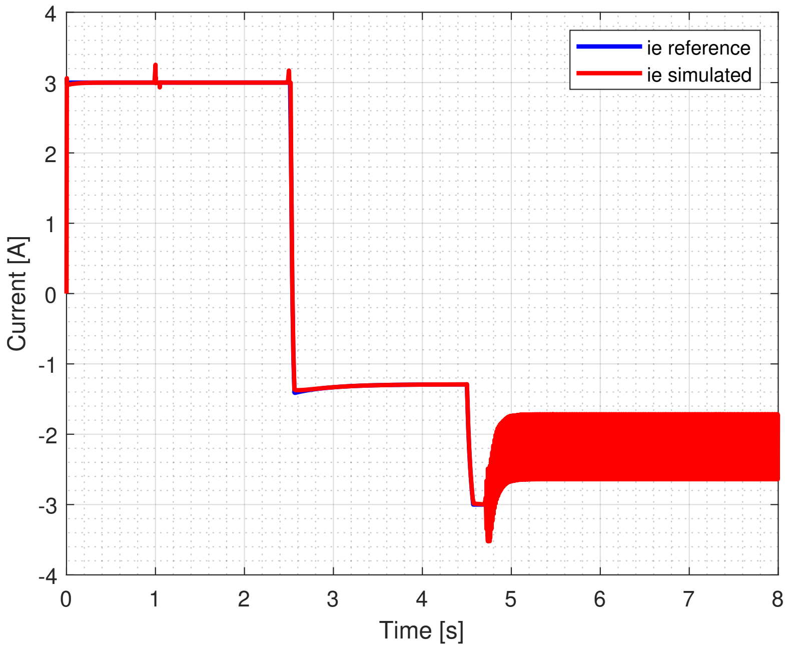

Figure 4.15: Excitation current.

## 4.4 RAMP RESPONSE

Fig. 4.16 shows the speed reference and the speed resulting from the simulation. Fig. 4.18 and Fig. 4.19 show, respectively, the direct and quadrature current reference and simulated. Same also for the excitation current in Fig. 4.20. Torque results are shown in Fig. 4.17.

For the same reasons as the linear model case, a ramp reference is taken into account to test the non-linear model. Comparing the results of the two models, it shows similar behaviour except for few differences: the torque, in Fig. 4.17, is not able to follow the reference (this issue is investigated in detail in Section 4.5).

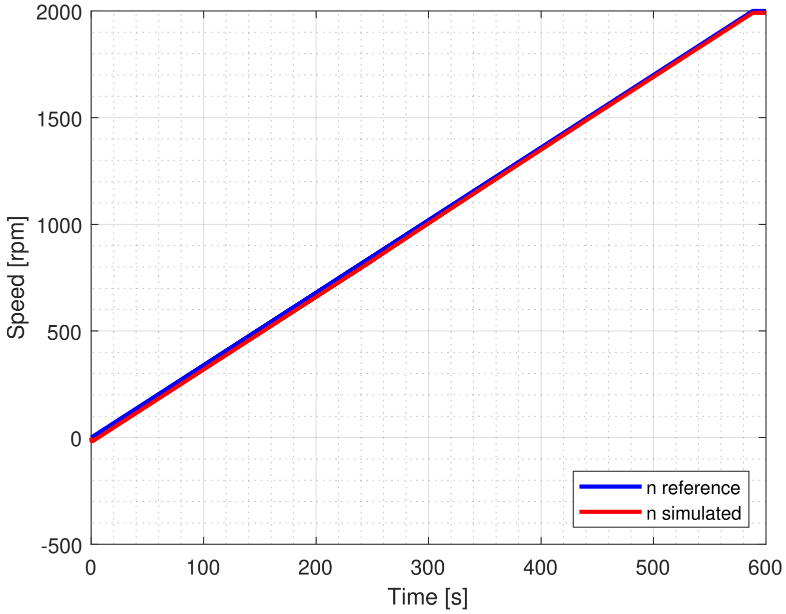

Figure 4.16: Speed.

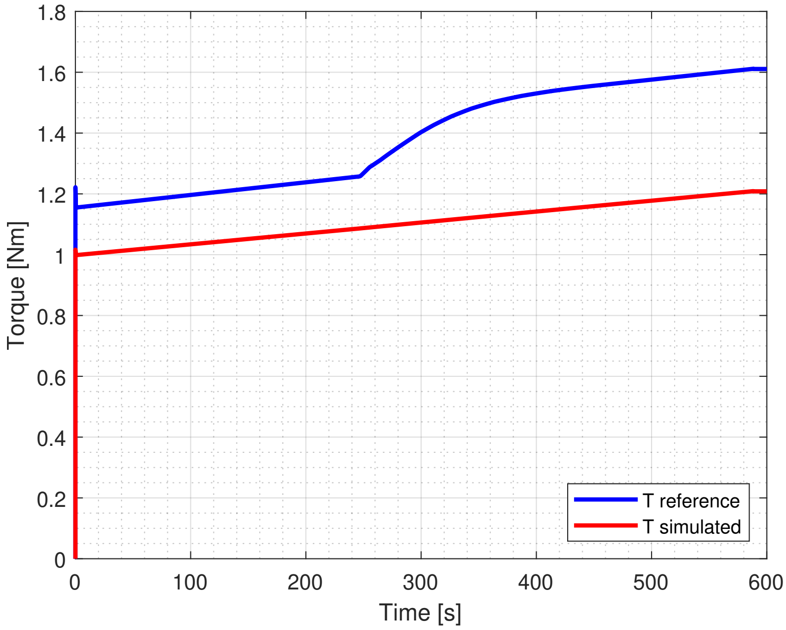

Figure 4.17: Torque.

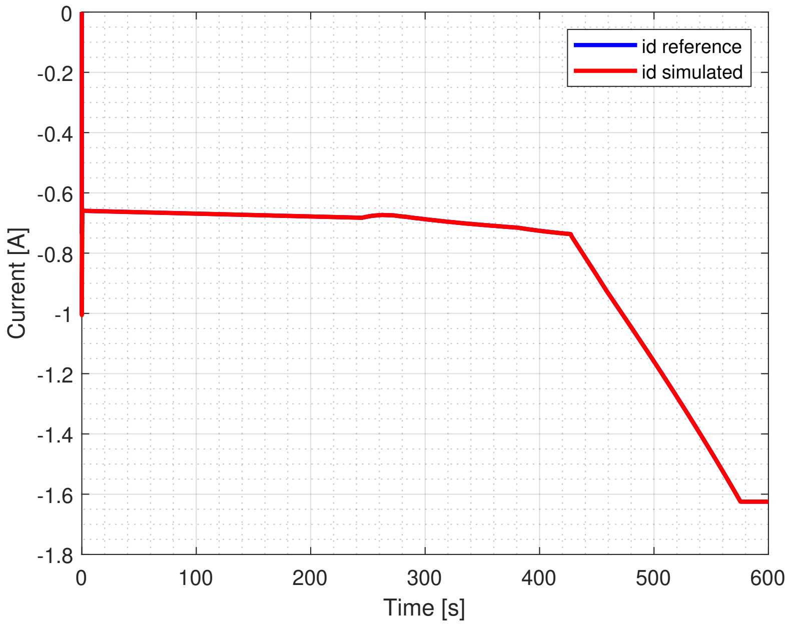

Figure 4.18: *d*-axis current.

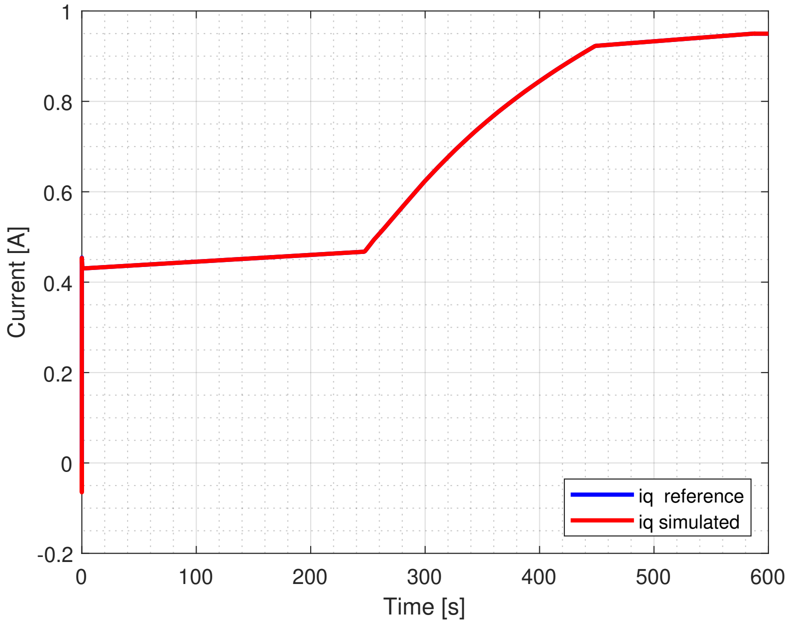

Figure 4.19: *q*-axis current.

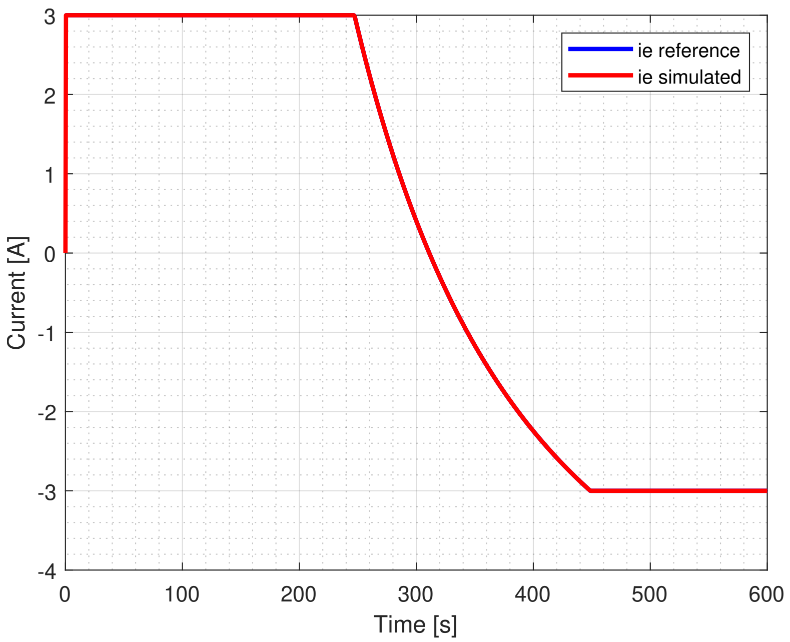

Figure 4.20: Excitation current.

## 4.5 TORQUE MAP IMPROVEMENT

In Fig. 4.17, torque simulation results are shown. As stated before, the results are not matching the reference and the reason is that MTPA trajectory is computed considering only torque and direct current working points.By modifying the map to also take into account the different excitation current operating points, the MTPA trajectory calculation is more accurate. Therefore, the MTPA block is modified obtaining a LUT with 2-D spline interpolation, as in Fig. 4.21:

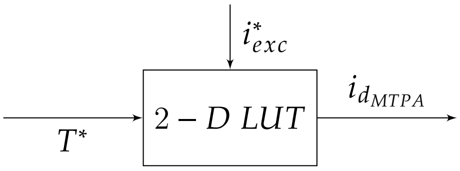

Figure 4.21: MTPA LUT improved block scheme.

The resulting map is showed in Fig. 4.22.

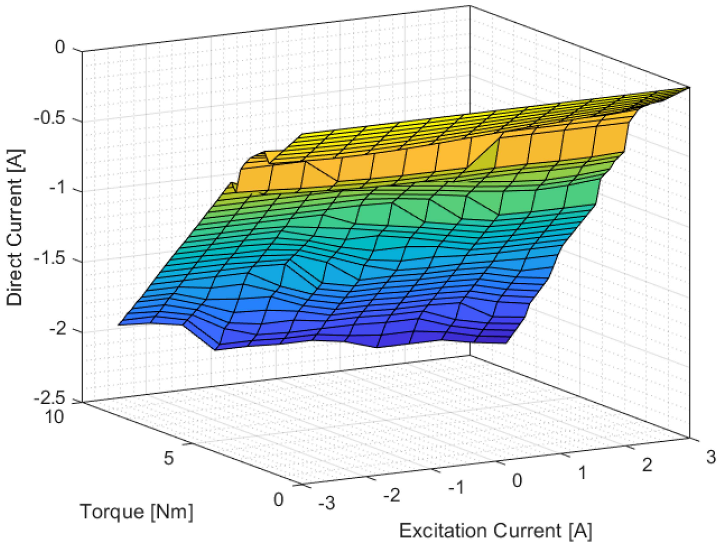

Figure 4.22: Map of the improved MTPA LUT.

The simulation results with the improved MTPA LUT are carried out: Fig. 4.23 shows the speed which exhibits the same behaviour of Fig: 4.16; moreover, torque, in Fig. 4.24, is able to follow the reference correctly. When the excitation current, in Fig. 4.27, starts to decrease, direct current (Fig. 4.25) increases. Then it decreases when the excitation current reaches the minimum value. The quadrature current (Fig. 4.26), instead, is always increasing.

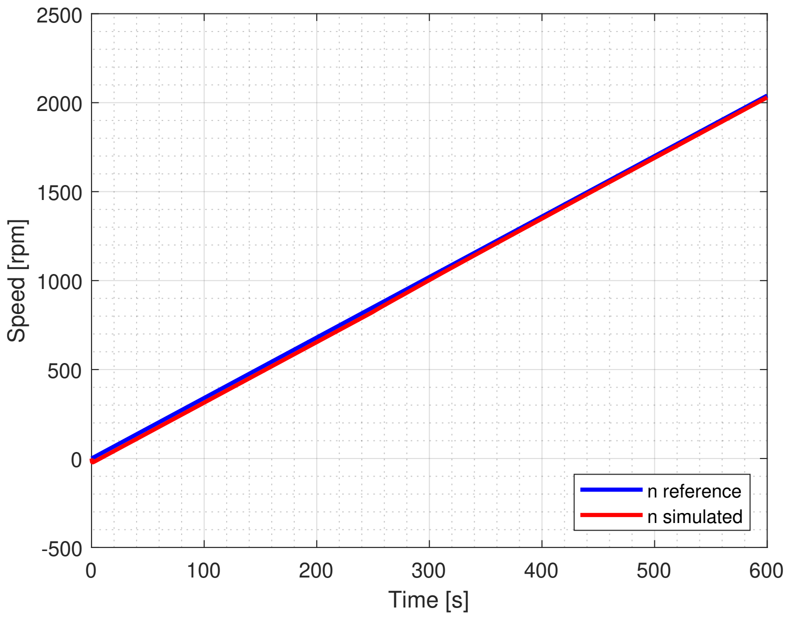

Figure 4.23: Speed.

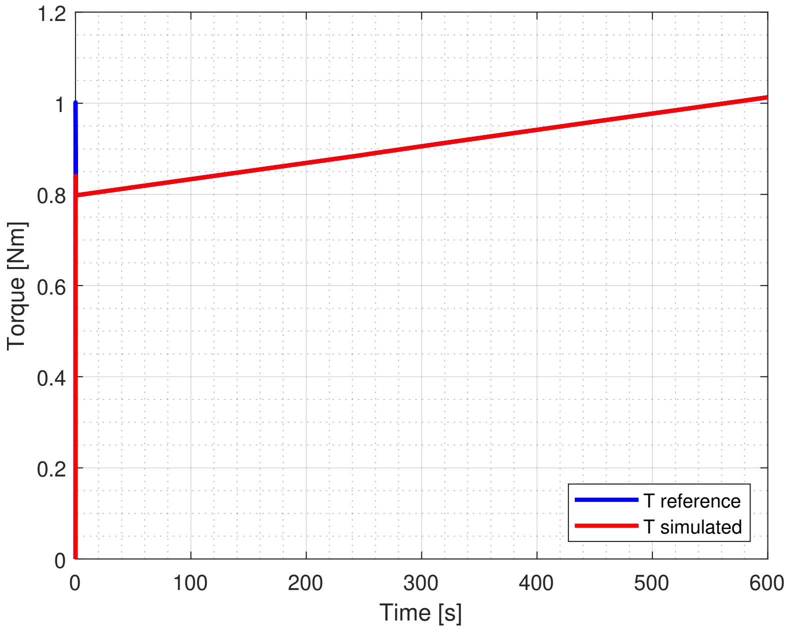

Figure 4.24: Torque.

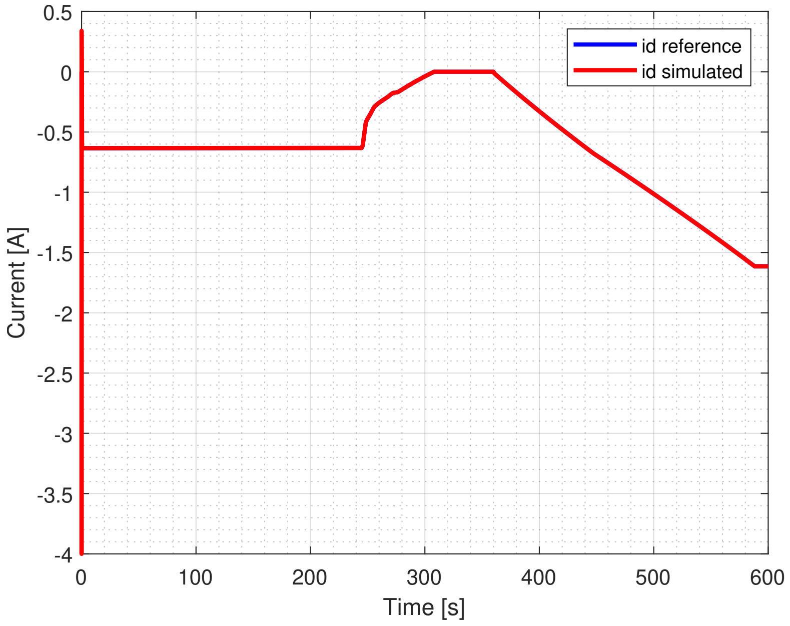

Figure 4.25: *d*-axis current.

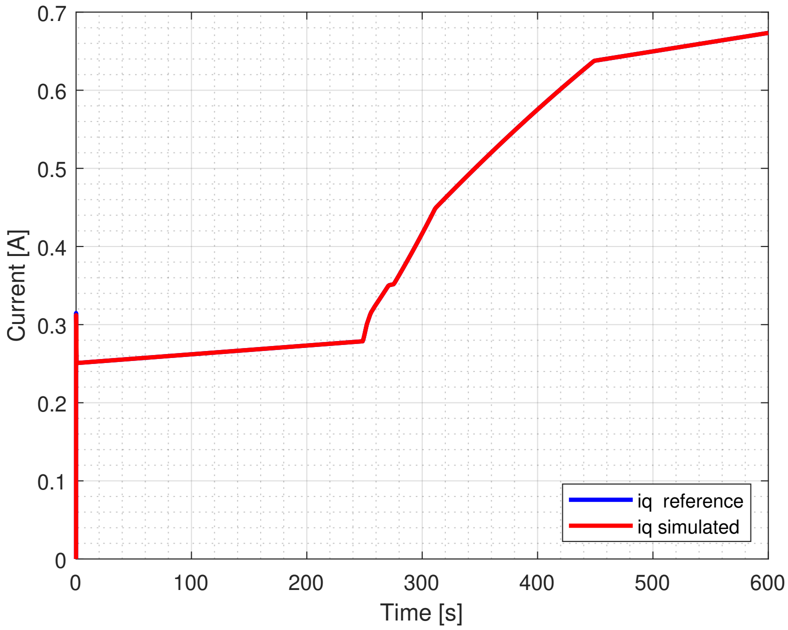

Figure 4.26: $q$-axis current.

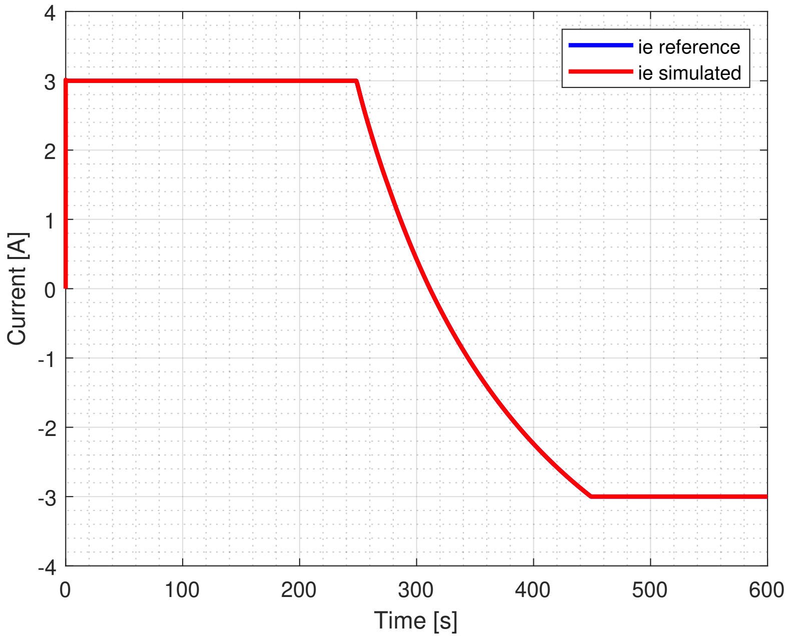

Figure 4.27: Excitation current.

## 4.6 VOLTAGE LOOP RESULTS

As described in the previous chapter, the design of the voltage loop has to follow precise rules of linearization, tuning and filtering. A way to verify the voltage loop design is to analyse the step response of the system showing the dynamical response of the loop. In particular, considering the speed and torque at steady state with a constant reference and using as voltage loop reference a step that goes from 200 V to 250 V, a behaviour similar to a first order dynamic response is expected [14]. Fig. 4.28 illustrates the results obtained by testing the HEPM motor model under these conditions. The voltage loop response follows well the reference. Therefore, the design of the voltage loop can be considered accurate.

The simulation outcome is obtained placing a filtering action on the voltage magnitude and on all the other quantities involved (speed and *dq*-axis currents) to ensure noise suppression.

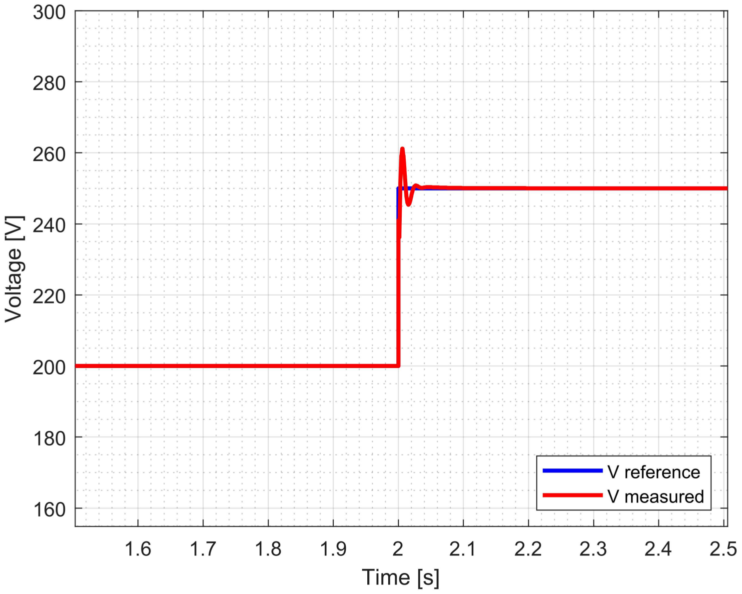

Figure 4.28: Voltage loop response given as input a 200-250 V step.

# 5

# dSPACE Simulation Results

Once the simulation results are satisfactory, the designed control system can be tested on a real HEPM motor prototype. This chapter discusses the testing process, describing the instrumentation on the test bench and the tool used an interface between the motor prototype and the control system.

## 5.1 TEST BENCH CONFIGURATION

Figure 5.1: Test bench.

The test bench used to test the designed control scheme is showed in Fig. 5.1. It consists of a master motor and a slave motor (in Fig. 5.2), each controlled by its own inverter. The excitation system comprises a power supply, an H-bridge inverter, brushes and slip rings. Additionally, there are sensors to measure the excitation current and the three-phase currents, along with a torque sensor mounted on the motor shaft (in Fig. 5.3).

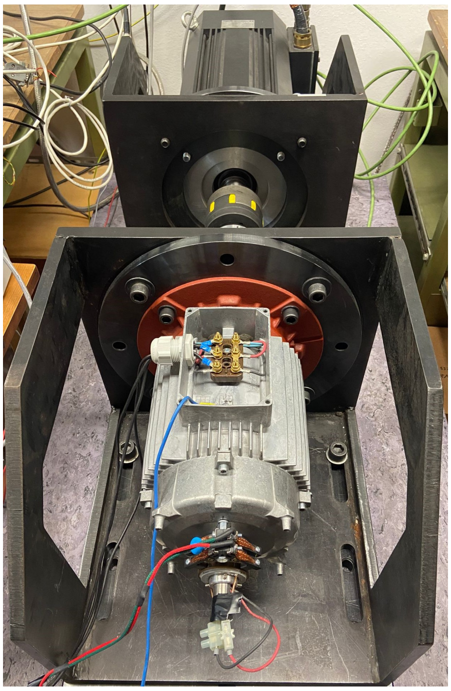

Figure 5.2: Motor.

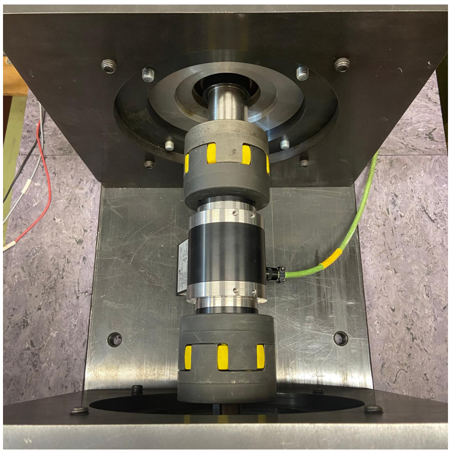

Figure 5.3: Torque sensor.

The designed control scheme communicates with the real motor prototype via a dSPACE MicroLab Box. The MATLAB Simulink model is converted into a

C code file and uploaded to the dSPACE system. Through the control interface of the dSPACE software, all parameters involved in the testing procedure can be monitored and controlled.

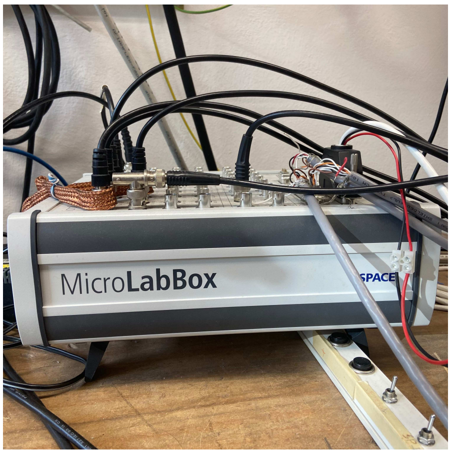

Figure 5.4: dSPACE MicroLab Box.

## 5.2 CONTROL SCHEME TESTING

In order to test the control on a real prototype, the first thing to do is to align the rotor. Rotor alignment involves adjusting the rotor position to align the $d$-axis rotor flux to the stator $a$-phase axis. This specific condition is satisfied when $\theta_{me} = 0$, as in Fig. 5.5. In this position, the flux linked by the $a$-phase is at its maximum, while the other two phases link a negative flux equal to half the value. Starting from a magnetostatic *Finite Element (FE)* simulation without currents in the stator winding, it is possible to verify the correct rotor alignment by calculating the no-load flux linkages and ensuring that the $d$-axis one $\Lambda_{d,0}$ is at its maximum, while the $q$-axis one $\Lambda_{q,0}$ is equal to zero. If $\Lambda_{q,0} \neq 0$, the rotor is not aligned and the rotation angle $\theta_{offset}$ required to align the rotor can be calculated [16]. For the motor under study, the alignment procedure starts by applying a positive stator $d$-axis current of $2.5\ A$ and the $q$-axis one set to zero to compute the offset angle. The same procedure is then repeated with a negative $d$-axis current to compute a second offset angle. The final offset angle is the arithmetic mean of the two. Once the motor is aligned, the testing procedure can start.

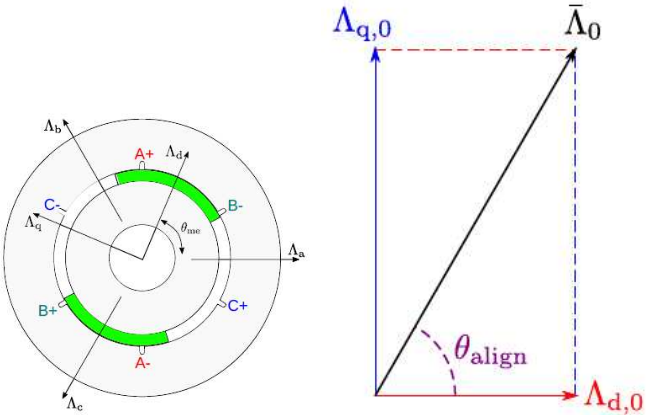

(a) Motor phases and flux linkage distributin. (b) No-Load flux with no alignment.

Figure 5.5: Reference $dq$-plane and rotor alignment.[16]

In this case, signals are acquired directly from the motor itself rather than being computed through FEA, so the motor model is no longer useful. The data acquisition is performed using a dSPACE MicroLab Box, shown in Fig. 5.4, which can read the signals from the motor.

The acquired signals need to be processed to become meaningful for the study. One of the signals acquired by dSPACE is the position angle $\theta$: the signal samples are collected by an encoder and then corrected by subtracting the offset angle calculated during the alignment procedure. Once the correct angle is computed, the mechanical and electrical speeds are calculated, along with the number of revolutions per minute $[rpm]$. Currents are also measured, and the signals are corrected by eliminating the sensor offset from the current measurement. During current acquisition, the signals are also monitored to prevent overcurrent faults. Specifically, if the acquired samples exceed a current threshold, the inverter is shut down. Sometimes, this safety value is briefly exceeded due to noise. In such cases, if the spikes exceed the limit current more than five times, the inverter is shut down. The torque is measured and corrected by removing the offset introduced by the sensor. The DC voltage is measured and corrected for any sensor offset.

After the acquisition stage, the measured speed is fed into the PI controller to generate the corresponding torque reference. From this, the MTPA strategy is used to compute the $d$-axis current reference, which is then added to the $d$-axis current reference recovered from the FW voltage regulator. The $q$-axis current is computed by applying the current limit circle condition. These $dq$-current references are the inputs to the PI regulator, which outputs the appropriate voltage to be supplied to the motor through the inverter. Consequently, the voltage is transformed using *Space Vector Modulation (SVM)*. The same procedure is applied to the excitation current: the reference is obtained from the optimal flux linkage computation and fed into the PI controller. The output voltage is then

supplied to an H-bridge inverter.
Now, the designed control scheme can be run and the motor's behavior can be analyzed. To view and adjust the motor parameters, the dSPACE ControlDesk interface can be configured accordingly. The configuration used for this testing is shown in Fig. 5.6.

Figure 5.6: ControlDesk of a dSPACE MicroLab Box.

The ControlDesk can be arranged to show all the type of signals, measurements, and parameters required for the test. In this case, the focus is initially placed on the enabling signals needed to start the inverter and cancel the offsets from the measurements. Then, the alignment procedure is carried out. Once the reference speed is set, the motor begins to rotate accordingly.

## 5.3 TEST RESULTS

The testing procedure is carried out, as in simulation, considering a step reference and then a ramp reference. In this case, the values of the reference signals are changed from the dSPACE ControlDesk during the test.

### 5.3.1 STEP REFERENCE

The step reference is taken into account: during the test, the amplitude of the step is increased by $50\ rpm$ each time, reaching at first the base speed and then the maximum available speed through FW. The results of this test are unsatisfactory: when the speed reference reaches the base speed, the $d$-axis current increases to $4\ A$, causing the motor to stop due to the overcurrent protection being triggered. In Fig. 5.7, the reference speed is reaching the base speed and, at the same time, the direct current is reaching the overcurrent limit. So the motor's behavior aligns with the simulations and, given the safety procedure applied on currents, the motor is shut down with no possibility to test it during FW operation.

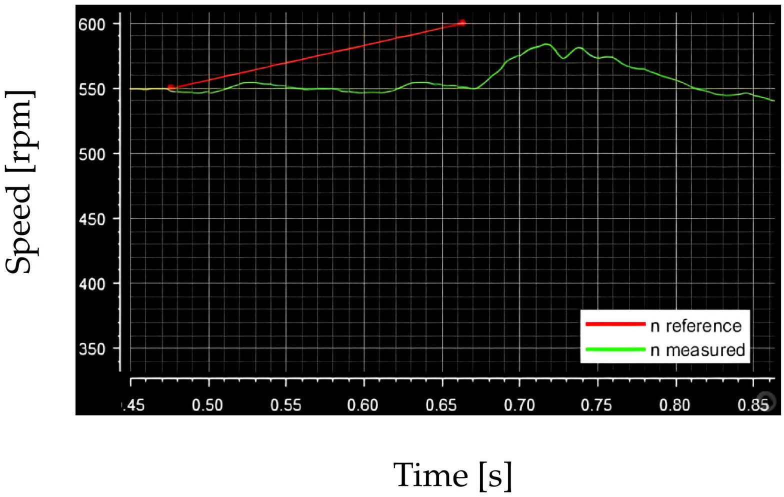

Figure 5.7: Speed.

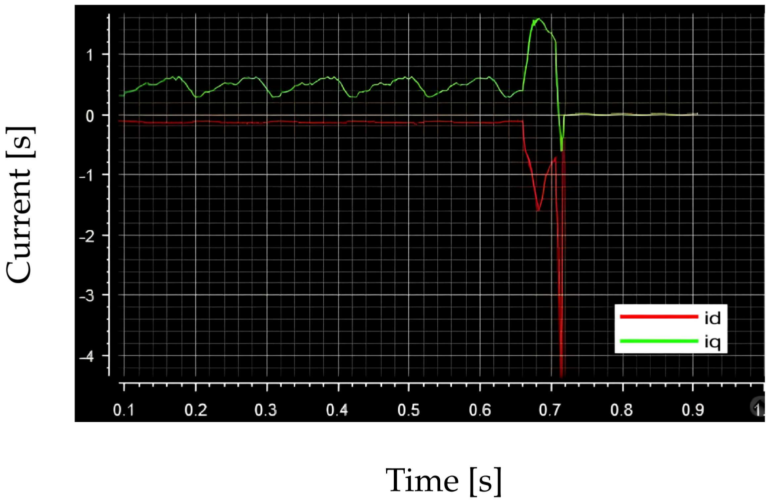

Figure 5.8: $d$-$q$ currents.

### 5.3.2 Ramp Reference

The second part of the testing procedure is carried out with a speed reference that behaves like a ramp. The direct and quadrature currents, in Fig. 5.11 and Fig. 5.12, are not showing spikes so the motor is able to work in the FW region. In Fig. 5.9 and Fig. 5.13 speed and excitation current are shown. The torque, in Fig. 5.10, is not able to follow correctly the refence as the MTPA strategy, described in Section 4.5,is used.

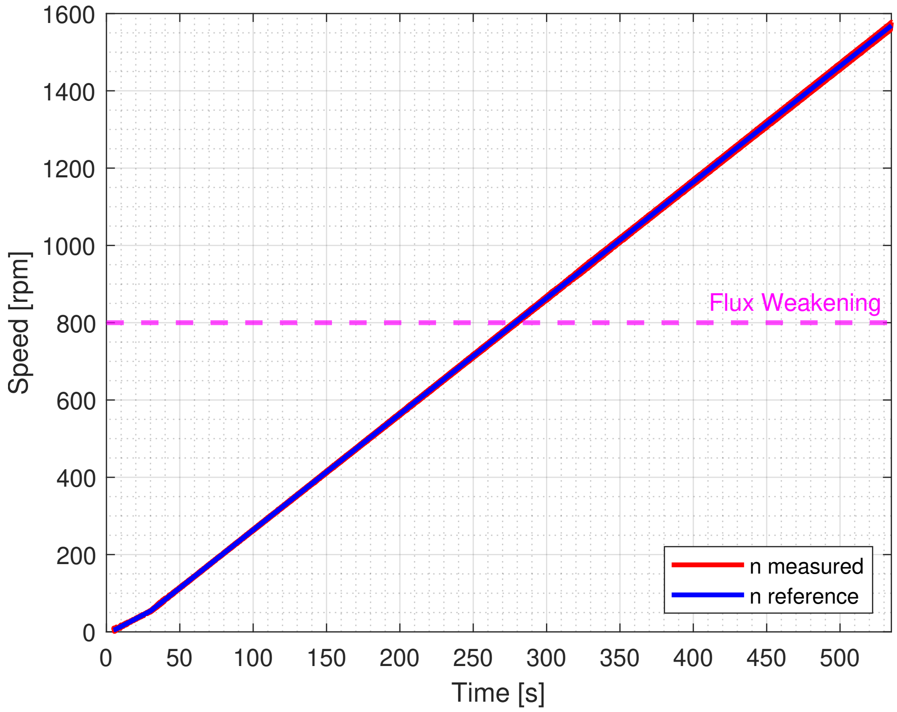

Figure 5.9: Speed.

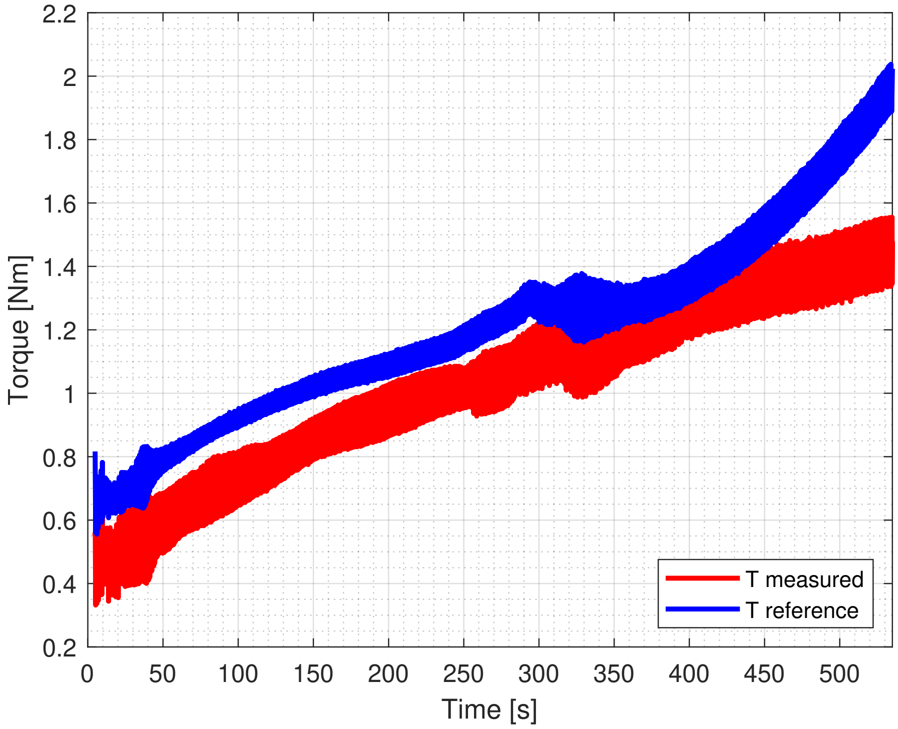

Figure 5.10: Torque.

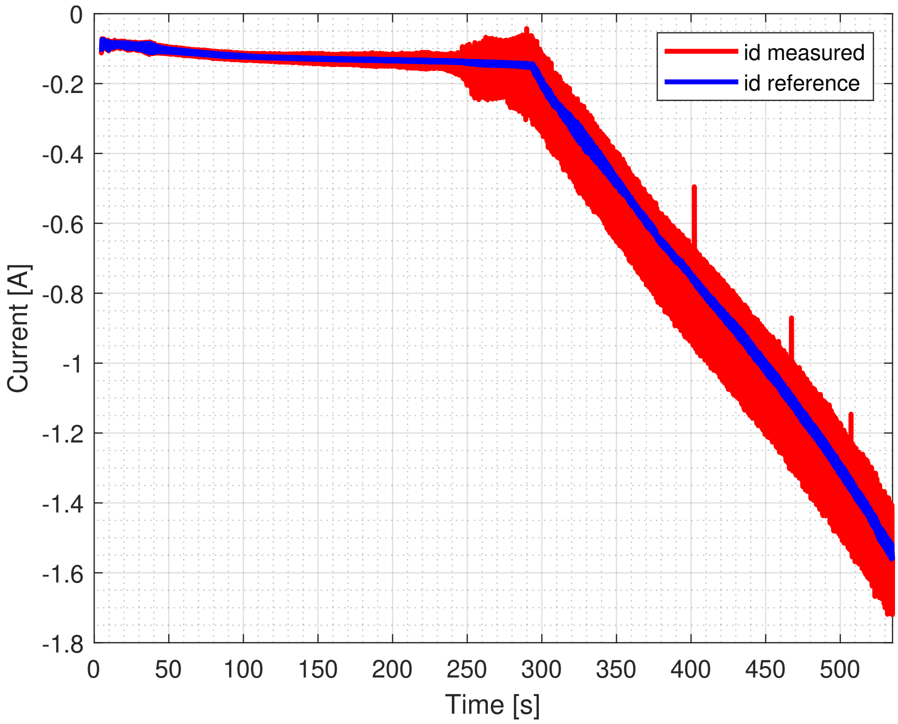

Figure 5.11: $d$-axis current.

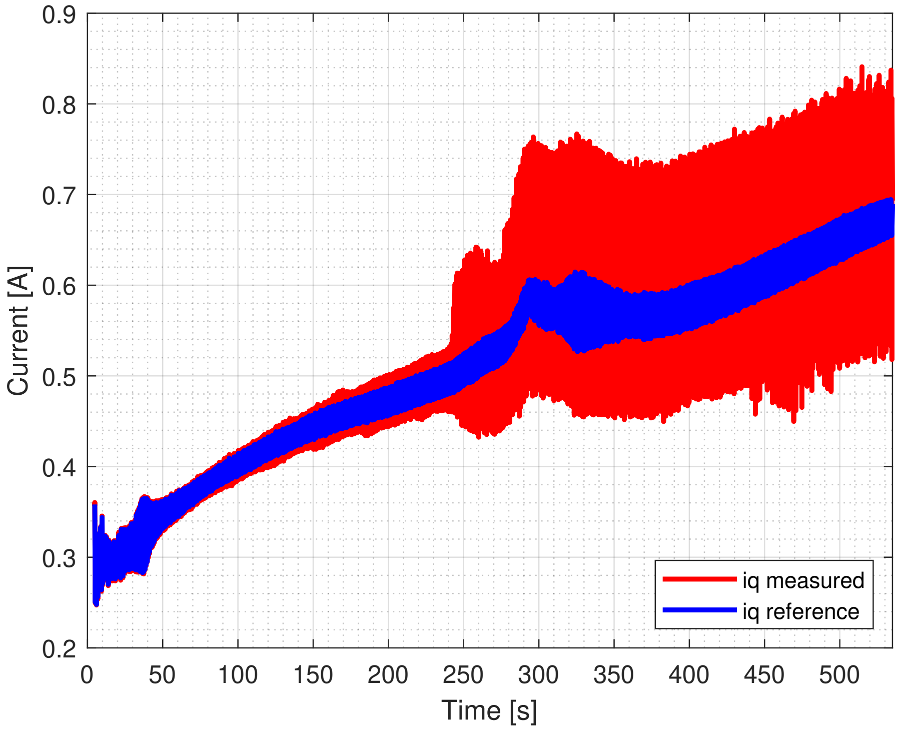

Figure 5.12: $q$-axis current.

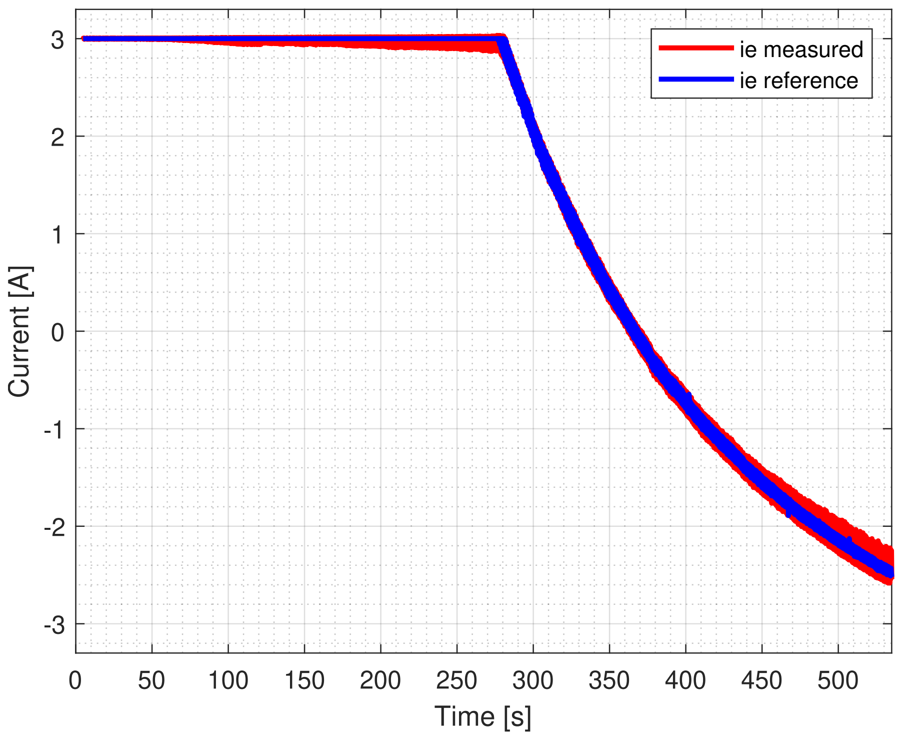

Figure 5.13: Excitation current.

### 5.3.3 Torque Map Improvement

Considering the improved version of the MTPA strategy (as detailed in Section 4.5), news tests are carried out. In Fig. 5.14 and Fig. 5.18 the speed and the excitation current are shown. The direct and quadrature current, in Fig. 5.16 and Fig. 5.17, exhibit behavior consistent with the simulation results. However, the torque (Fig. 5.15), instead, still does not align perfectly with the reference.

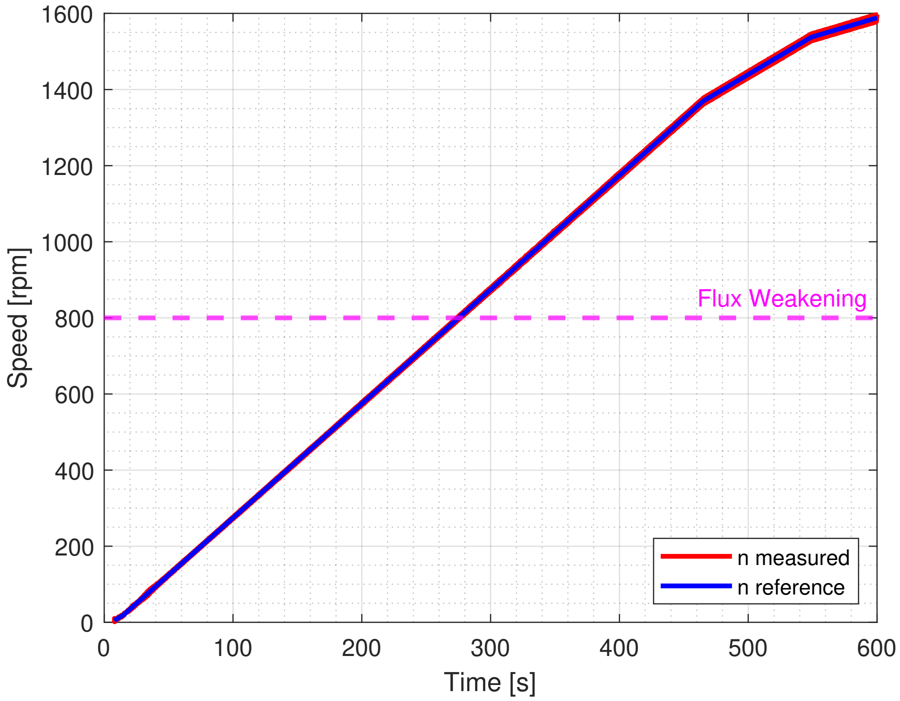

Figure 5.14: Speed.

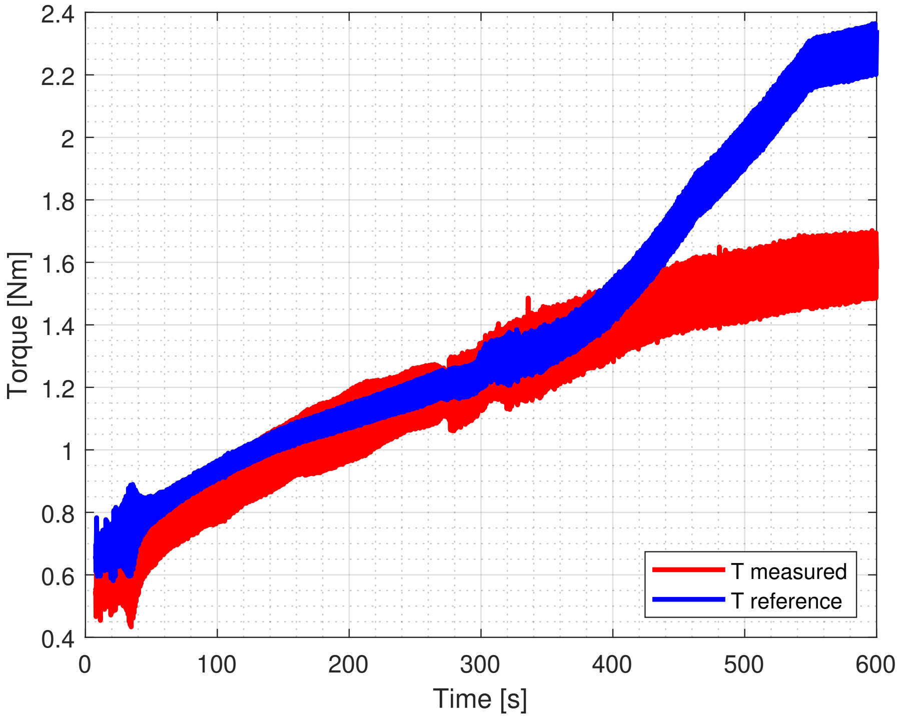

Figure 5.15: Torque.

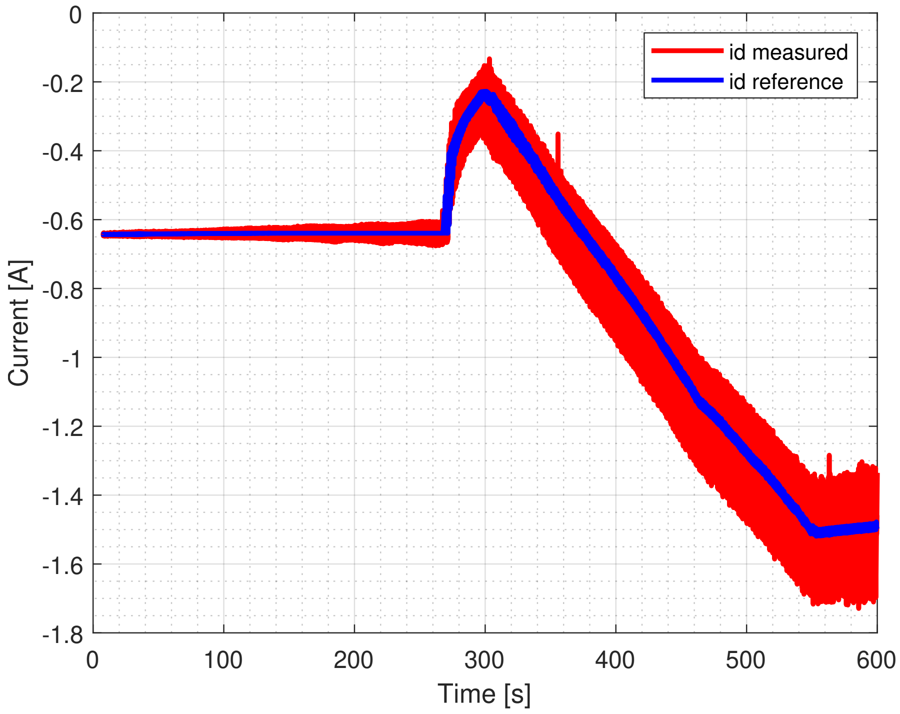

Figure 5.16: *d*-axis current.

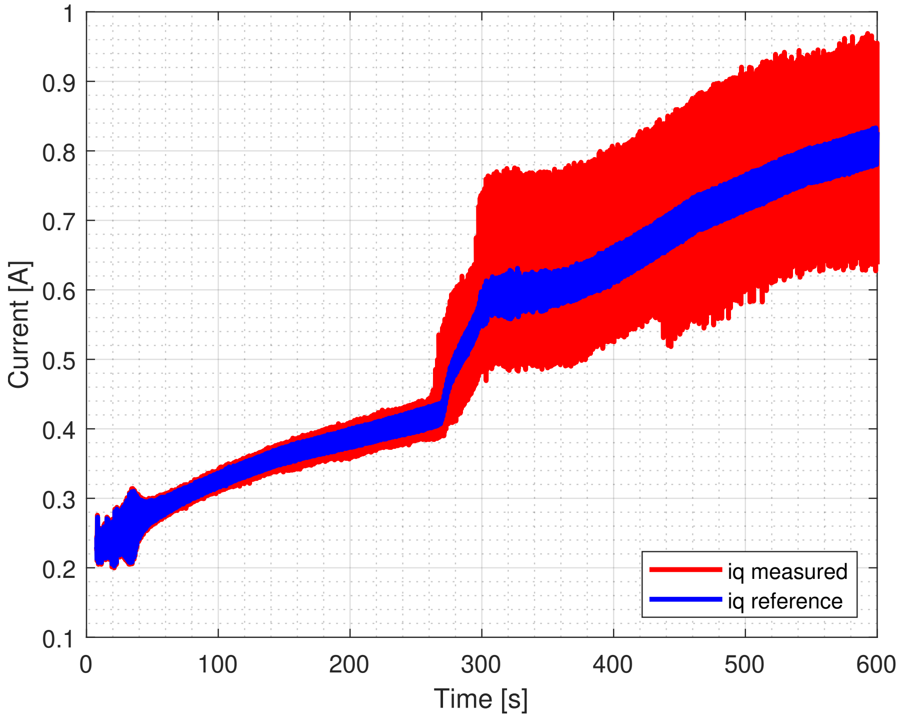

Figure 5.17: *q*-axis current.

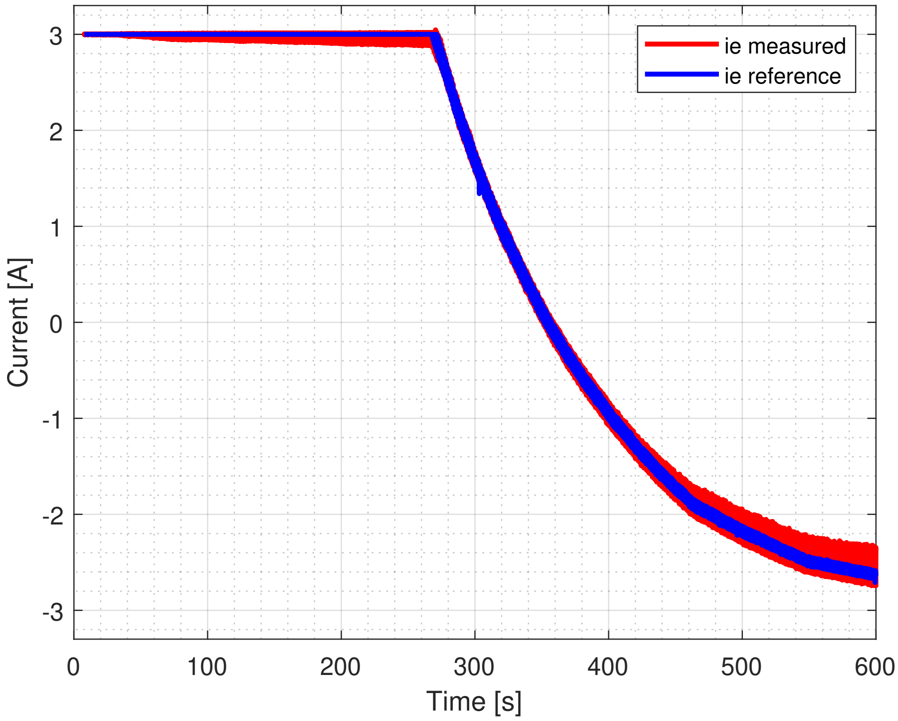

Figure 5.18: Excitation current.

### 5.3.4 ALIGNMENT PROCEDURE IMPROVEMENT

Since the torque reference is generated by the speed controller, which is linked to the alignment procedure, the angle $\theta$ can influence the torque behavior. For this reason, the alignment procedure and the resulting angle are deeply investigated. The results shown in Section 5.3.2, obtained with the basic MTPA strategy, display a $\theta$ angle comprised in a range of $[-4, 3]$ $rad$, as in Fig. 5.19.

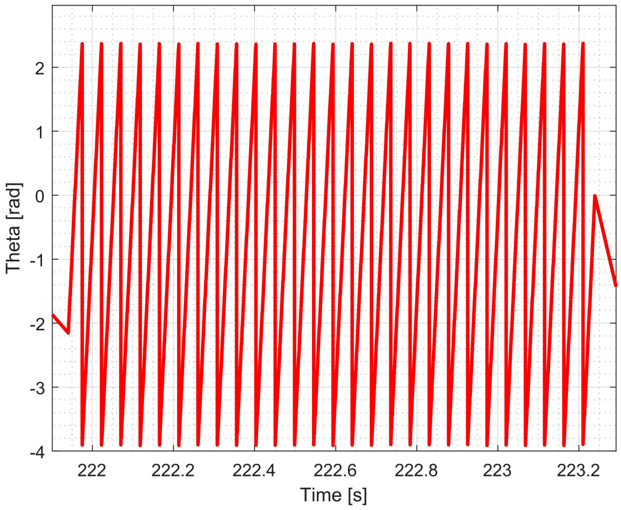

Figure 5.19: Resulting angle of a wrong alignment procedure (with basic MTPA).

Performing again the alignment procedure, the range of the angle changes to $[-1, 6]$ *rad*, as in Fig. 5.20.

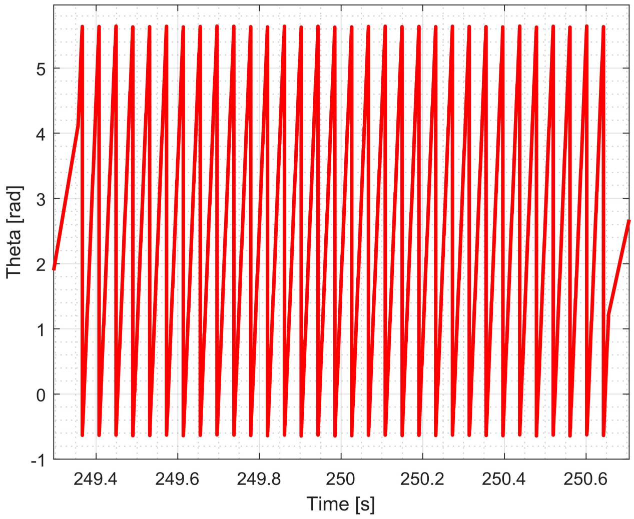

Figure 5.20: Resulting angle of a correct alignment procedure (with basic MTPA).

Measurements obtained with the $\theta$ angle in Fig. 5.20 prove to be an improvement compared to the previous one: speed is showed in Fig. 5.21, excitation current in Fig. 5.25; direct and quadrature current are showed in Fig. 5.23 and Fig. 5.24 while torque in Fig. 5.22.

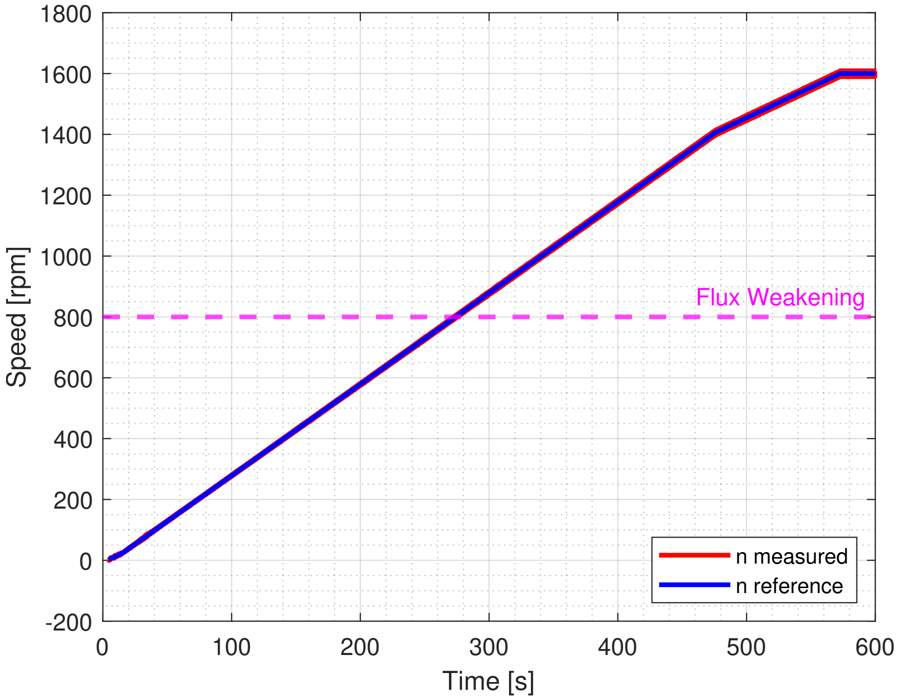

Figure 5.21: Speed.

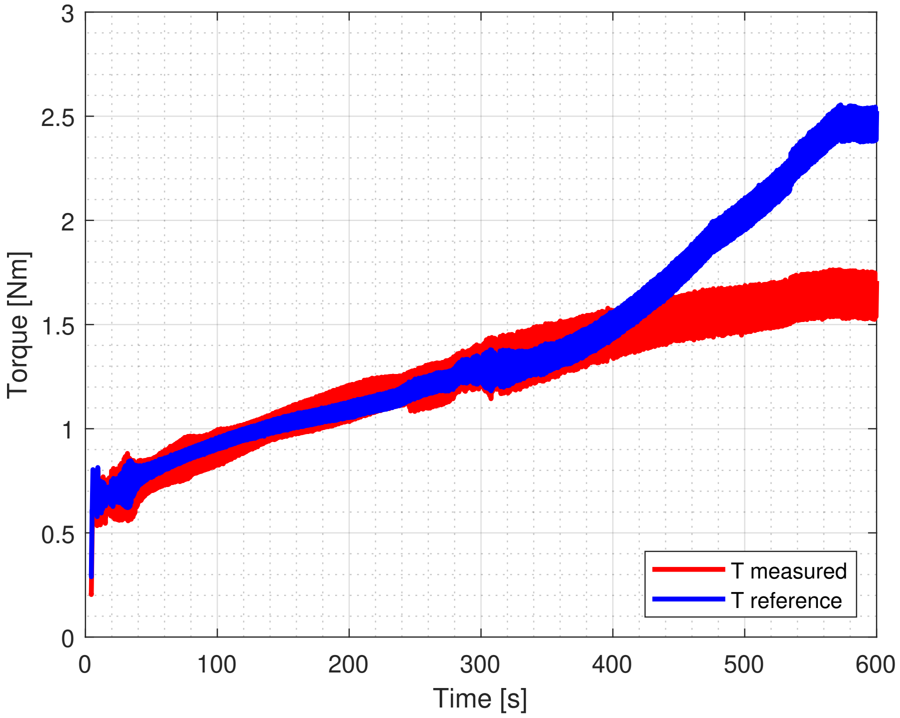

Figure 5.22: Torque.

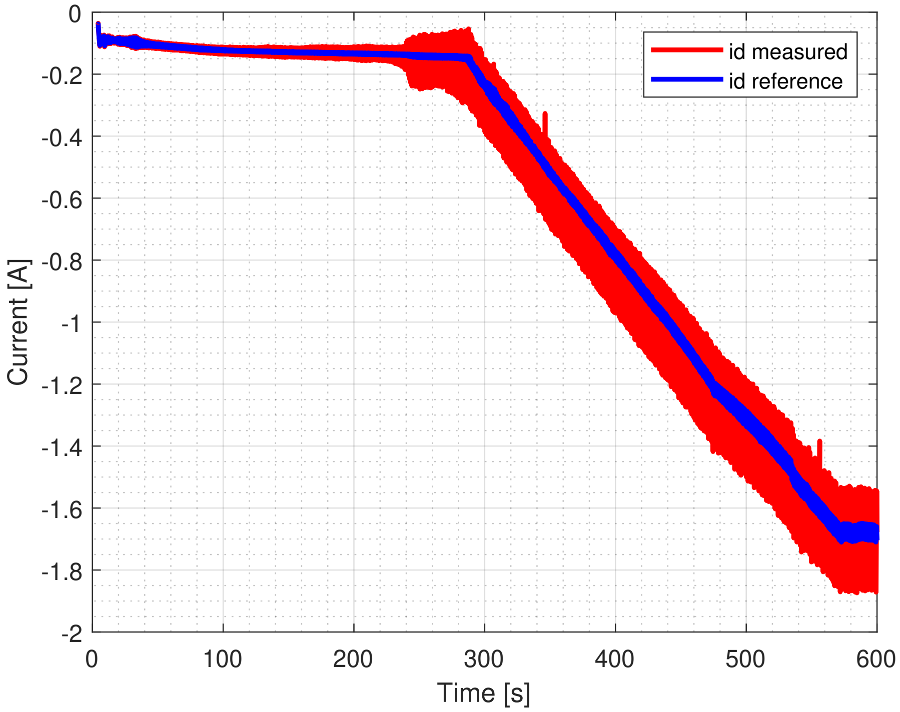

Figure 5.23: *d*-axis current.

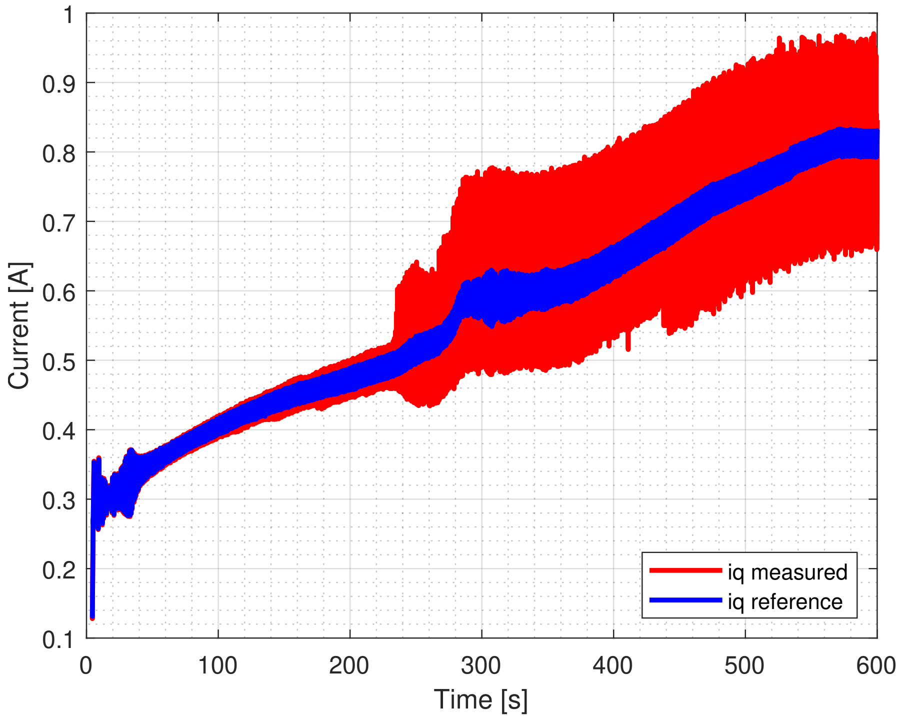

Figure 5.24: $q$-axis current.

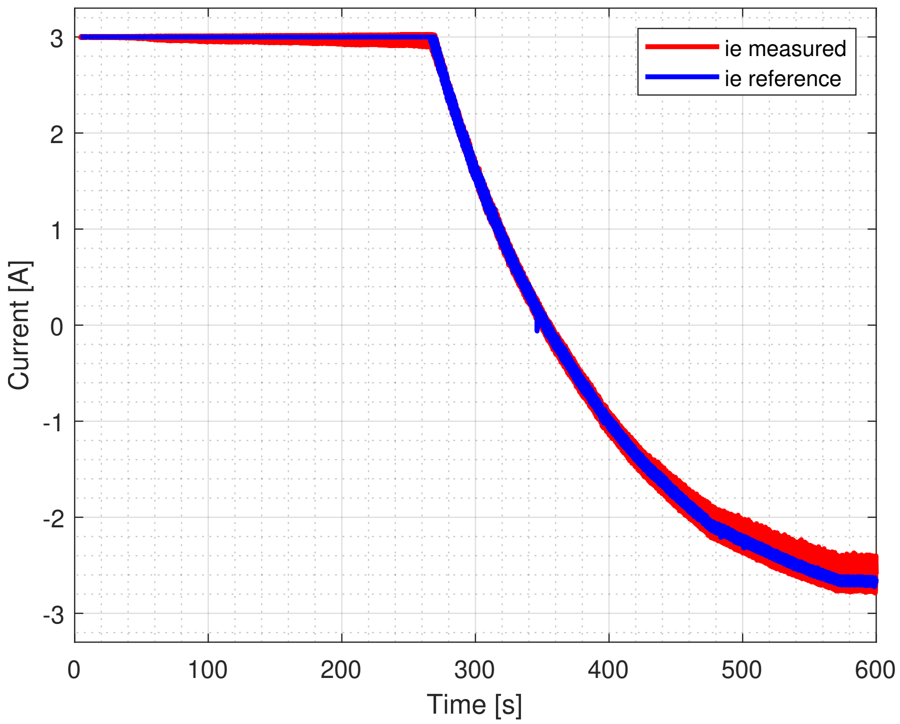

Figure 5.25: Excitation current.

The results obtained with the improved MTPA (Section 5.3.3) display an angle between $[0, -7]$ $rad$ as in Fig. 5.26.

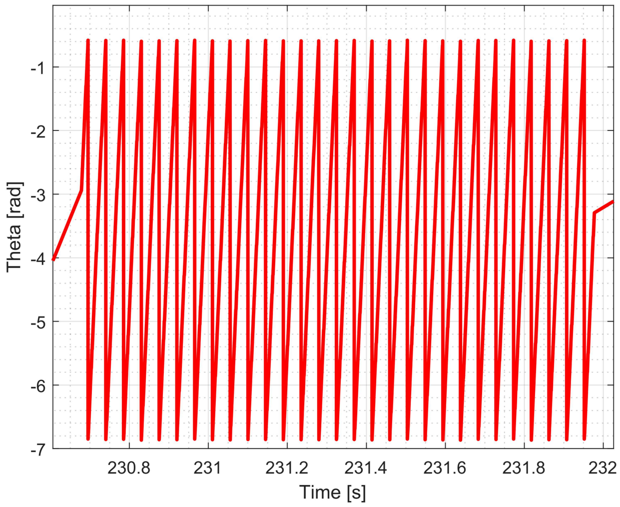

Figure 5.26: Resulting angle of a wrong alignment procedure (with modified MTPA).

Considering the correct alignment procedure (with theta in a range of about $-1\ rad$ and $5\ rad$) with the new maps for the MTPA strategy, the behaviour of the torque is showed in Fig. 5.28. In Fig. 5.27 and Fig. 5.31, speed ane excitation current are showed. Direct and quadrature currents are showed in Fig. 5.29 and Fig. 5.30.

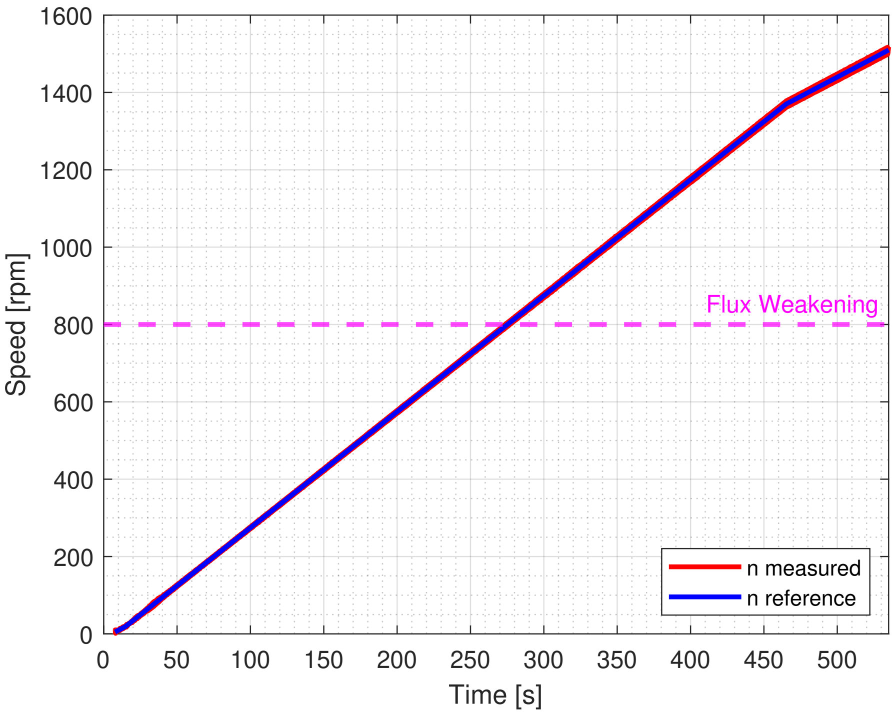

Figure 5.27: Speed.

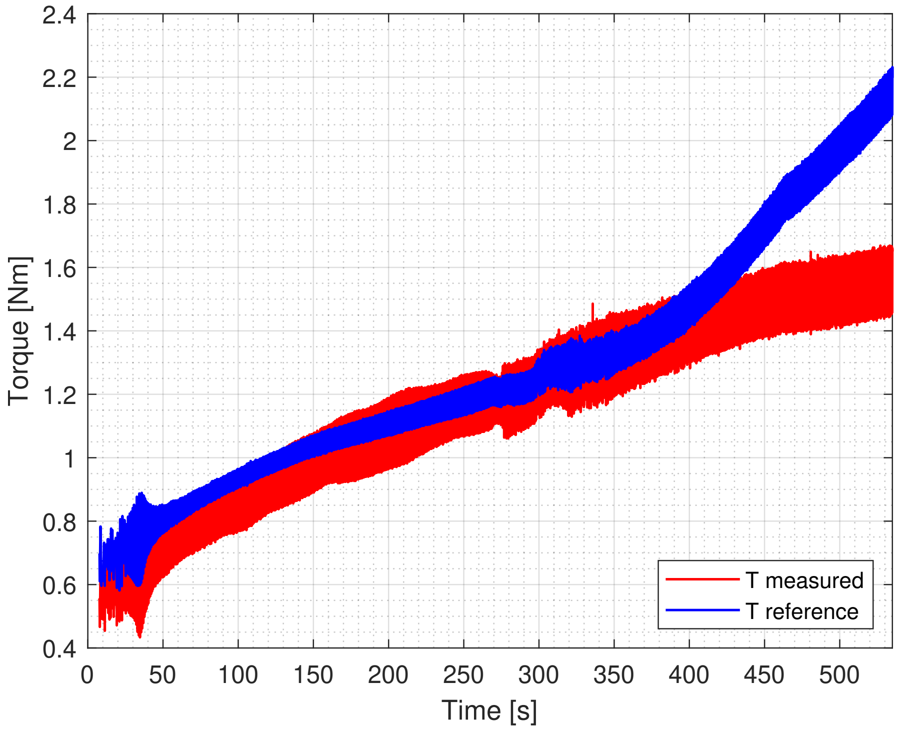

Figure 5.28: Torque.

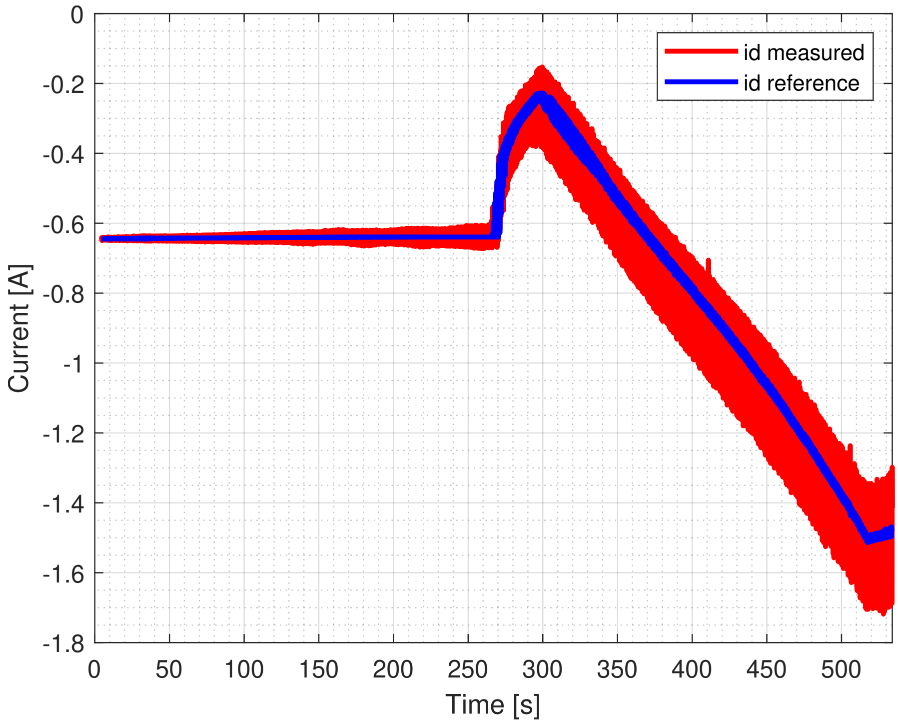

Figure 5.29: $d$-axis current.

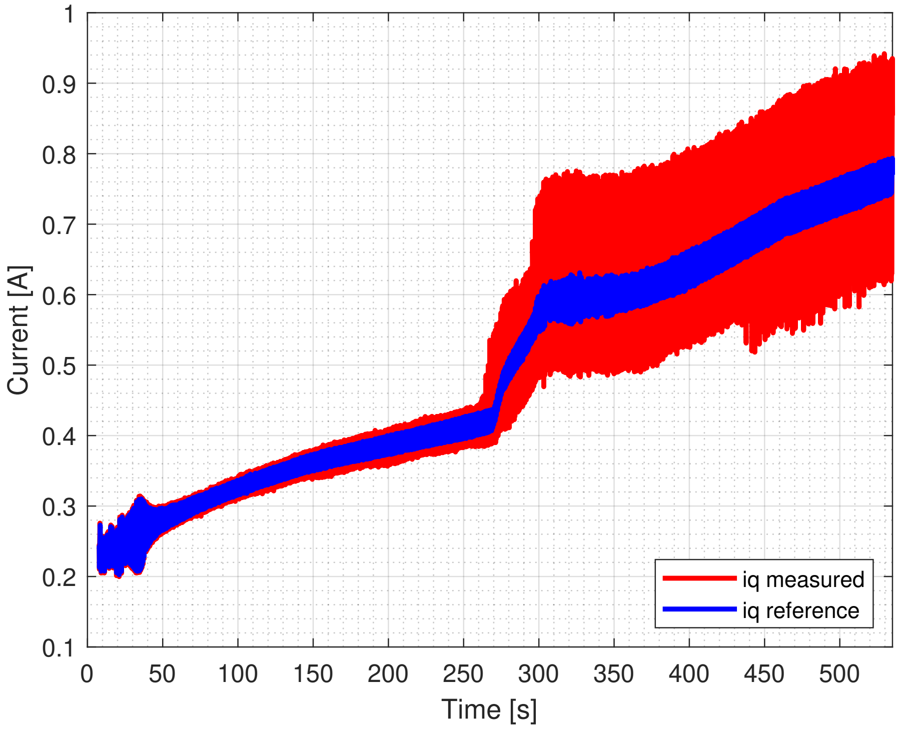

Figure 5.30: $q$-axis current.

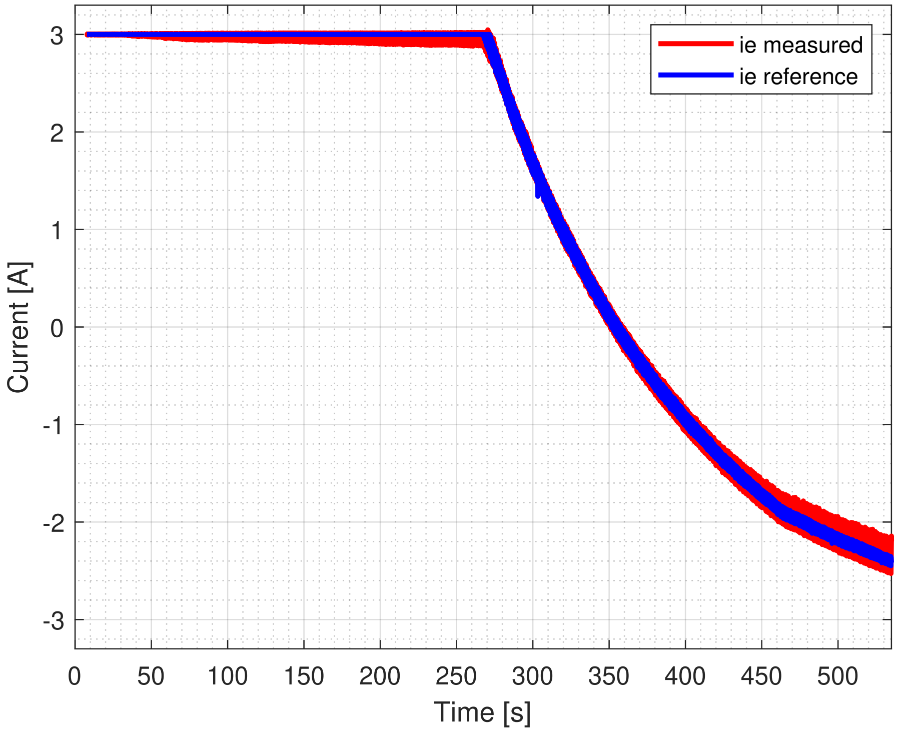

Figure 5.31: Excitation current.

Combining a correct alignment procedure with the improved MTPA strategy, torque has a better performance: it is able to follow the reference until the maximum feasible speed is reached. Both correction have to be implemented in order to obtain good results during tests.

# Conclusions

This thesis presented the design, modeling, and experimental validation of a control drive for a *Hybrid Excited Permanent Magnet (HEPM)* motor. The research successfully addressed both theoretical and practical challenges, with the aim of improving motor performance while reducing reliance on rare earth materials.

The key advantage of the HEPM motor, its ability to adjust rotor flux, was demonstrated to be an effective solution for optimizing speed, torque, and power density. Through the development of linear and non-linear models, it was possible to simulate motor behavior accurately and design a control strategy that meets the demands of *Flux Weakening (FW)* operation.

An enhanced *Maximum Torque Per Ampere (MTPA)* strategy was also developed, taking into account the excitation current, which led to significant improvements in both simulation and testing. Experimental results confirmed the validity of the proposed control scheme, demonstrating strong alignment with the simulation data.

Moreover, the improvement of the rotor alignment procedure resulted in further performance enhancements, underlining the importance of precise alignment in the overall efficiency of the motor.

In conclusion, the combination of the optimized MTPA strategy and the improved alignment procedure yielded satisfactory performance, confirming the HEPM motor as a viable alternative for high-performance applications. Future research could explore additional improvements in control strategies and further reduce dependency on rare earth materials, contributing to more sustainable motor designs.

# Bibliography

[1] Rebecca Matulka. *The History of the Electric Car*. 2024. URL: `https://www.energy.gov/articles/history-electric-car`.

[2] Idaho National Laboratory. "History of Electric Cars". In: *Idaho National Laboratory's website* (2020).

[3] Dipesh Thakur. *Electric Vehicle Architecture and EV Powertrain Components*. 2021. URL: `https://e-vehicleinfo.com/electric-vehicle-architecture-ev-powertrain-components/`.

[4] Iman Aghabali; Jennifer Bauman; Phillip J. Kollmeyer; Yawei Wang; Berker Bilgin; Ali Emadi. *800-V Electric Vehicle Powertrains: Review and Analysis of Benefits, Challenges, and Future Trends*. 2020.

[5] HQL INduction Equipment Co. *Induction preheating and post welding*. 2021. URL: `https://it.dw-inductionheater.com/prodotto/statore-e-rotore-calettabili-ad-induzione`.

[6] ENNENG. *What is the difference between IPM and SPM motor?* URL: `https://enmotor.com/what-is-the-difference-between-ipm-and-spm-motor/`.

[7] Maria Alejandra León; Tian Daphne. *The rare earth problem: Sustainable sourcing and supply chain challenges*. 2023. URL: `https://www.circularise.com/blogs/the-rare-earth-problem-sustainable-sourcing-and-supply-chain-challenges#:~:text=REEs%20are%20extracted%20through%20extensive,and%20the%20disruption%20of%20ecosystems.`.

[8] F. Filippini; M. Pastura; N. Bianchi. "PM and PM-less Motors for Electric Vehicles: a Comparative Analysis". In: (2024).

[9] D. Michieletto; L. Cinti; N. Bianchi. "Hybrid Excitation PM Synchronous Motors: Part II — Finite Element Analysis". In: *IEEE TRANSACTIONS ON ENERGY CONVERSION,* 37.1 (2022).

[10] D. Michieletto; L. Cinti; N. Bianchi. "Hybrid Excitation PM Synchronous Motors: Part I — Per Unit Analysis". In: *IEEE TRANSACTIONS ON ENERGY CONVERSION,* 37.1 (2022).

[11] L. Cinti; P. G. Carlet; L. Ortombina; N. Bianchi. "Flux-Weakening Control of Hybrid-Excited Permanent Magnet Synchronous Motors". In: (2022).

[12] N. Bianchi; P. G. Carlet; L. Cinti; L. Ortombina. "A Review about Flux-Weakening Operating Limits and Control Techniques for Synchronous Motor Drives". In: 15.1930 (2022).

[13] P. G. Carlet; L. Cinti; L. Ortombina; N. Bianchi. "Dynamic model for HEPM motors including the nonlinear magnetic characteristics". In: (2023).

[14] N. Bedetti; S. Calligaro. "Analytical Design and Autotuning of Adaptive Flux-Weakening Voltage Regulation Loop in IPMSM Drives With Accurate Torque Regulation". In: 56.1 (2020).

[15] J. Jacob; O. Bottesi; S. Calligaro; R. Petrella. "Design Criteria for Flux Weakening Contr ol Bandwidth and Voltage Margin in IPMSM Drives Considering Transient Conditions". In: (2021).

[16] L. Cinti; D. Michieletto; N. Bianchi; M. Bertoluzzo. "Hybrid Excited Permanent Magnet Motor: Analytical Sizing, Finite Element Analysis and Tests". In: (2023).